

Automated seafloor massive sulfide detection through integrated image segmentation and geophysical data analysis: Revisiting the TAG hydrothermal field

Amir Haroon¹, Hendrik Paasche², Sebastian Graber³, Sven Petersen¹, Eric Attias⁴, Marion Jegen¹, Romina Gehrman⁵, Sebastian Hölz¹, and Meike Klischies⁶

¹GEOMAR

²Unknown

³GEOMAR Helmholtz Centre of Ocean Research Kiel

⁴Institute for Geophysics

⁵Dalhousie University

⁶north.io GmbH

September 29, 2023

Abstract

Accessible seafloor minerals located near mid-ocean ridges are noticed to mitigate projected metal demands of the net-zero energy transition, promoting growing research interest in quantifying global distributions of seafloor massive sulfides (SMS). Mineral potentials are commonly estimated using geophysical and geological data that lastly rely on additional confirmation studies using sparsely available, locally limited, seafloor imagery, grab samples, and coring data. This raises the challenge of linking in-situ confirmation data to geophysical data acquired at disparate spatial scales to obtain quantitative mineral predictions. Although multivariate datasets for marine mineral research are incessantly acquired, robust, integrative data analysis requires cumbersome workflows and experienced interpreters. Here, we introduce an automated two-step machine learning approach that integrates automated mound detection with geophysical data to merge mineral predictors into distinct classes and reassess marine mineral potentials for distinct regions. The automated workflow employs a U-Net convolutional neural network to identify mound-like structures in bathymetry data and distinguishes different mound classes through classification of mound architectures and magnetic signatures. Finally, controlled source electromagnetic data is utilized to reassess predictions of potential SMS volumes. Our study focuses on the Trans-Atlantic Geotraverse (TAG) area, which is amid the most explored SMS area worldwide and includes 15 known SMS sites. The automated workflow classifies 14 of the 15 known mounds as exploration targets of either high- or medium-priority. This reduces the exploration area to less than 7% of the original survey area from 49 km² to 3.1 km².

Hosted file

974737_0_supp_11427291_s111wc.docx available at <https://authorea.com/users/557261/articles/669649-automated-seafloor-massive-sulfide-detection-through-integrated-image-segmentation-and-geophysical-data-analysis-revisiting-the-tag-hydrothermal-field>

Automated seafloor massive sulfide detection through integrated image segmentation and geophysical data analysis: Revisiting the TAG hydrothermal field

Amir Haroon^{1,2}, Hendrik Paasche³, Sebastian Graber^{1,4}, Sven Petersen¹, Eric Attias^{5,6}, Marion Jegen¹, Romina Gehrman⁷, Sebastian Hölz¹, Meike Klischies^{1,8}

¹ Helmholtz Centre for Ocean Research, GEOMAR Kiel, Wischhofstr. 1-3, 24148, Kiel Germany

² Hawaii Institute of Geophysics and Planetology, School of Ocean and Earth Science and Technology, University of Hawai'i at Manoa, Honolulu, HI, USA

³ UFZ Helmholtz Centre for Environmental Research, Leipzig, Germany

⁴ Helmut-Schmidt Uni Hamburg

⁵ Institute for Geophysics, Jackson School of Geosciences, The University of Texas at Austin, Austin, TX, USA

⁶ Department of Geology and Geophysics, Woods Hole Oceanographic Institution, Woods Hole, Massachusetts, USA

⁷ Dalhousie University, 6299 South St, Halifax, NS, B3H 4R2, Canada

⁸ North.io GmbH, Einsteinstraße 1, 24118 Kiel, Germany

ORCID IDs

Amir Haroon: 0000-0001-5138-6730; Hendrik Paasche: 0000-0003-1814-0645; Sebastian Graber: 0000-0003-1154-6968; Eric Attias: 0000-0003-4308-1683; Romina Gehrman: 0000-0002-3099-2771; Sebastian Hölz: 0000-0003-2839-9394; Marion Jegen: 0000-0001-6307-8428; Sven Petersen: 0000-0002-5469-105X; Meike Klischies: 0000-0003-4319-4573

Key Points

- Developed two-step machine learning workflow to identify mound structures in bathymetry and classify their origins based on auxiliary data.
- Substantial increase of potential SMS edifices detected within the TAG hydrothermal field distributed within latitudinal bands.
- SMS mineral potential is likely lower than perviously assumed due to heterogeneously distributed mineralization within mounds.

30 **Abstract**

31 Accessible seafloor minerals located near mid-ocean ridges are noticed to mitigate projected metal
32 demands of the net-zero energy transition, promoting growing research interest in quantifying global
33 distributions of seafloor massive sulfides (SMS). Mineral potentials are commonly estimated using
34 geophysical and geological data that lastly rely on additional confirmation studies using sparsely
35 available, locally limited, seafloor imagery, grab samples, and coring data. This raises the challenge of
36 linking in-situ confirmation data to geophysical data acquired at disparate spatial scales to obtain
37 quantitative mineral predictions. Although multivariate datasets for marine mineral research are
38 incessantly acquired, robust, integrative data analysis requires cumbersome workflows and experienced
39 interpreters. Here, we introduce an automated two-step machine learning approach that integrates
40 automated mound detection with geophysical data to merge mineral predictors into distinct classes and
41 reassess marine mineral potentials for distinct regions. The automated workflow employs a U-Net
42 convolutional neural network to identify mound-like structures in bathymetry data and distinguishes
43 different mound classes through classification of mound architectures and magnetic signatures. Finally,
44 controlled source electromagnetic data is utilized to reassess predictions of potential SMS volumes.
45 Our study focuses on the Trans-Atlantic Geotraverse (TAG) area, which is amid the most explored
46 SMS area worldwide and includes 15 known SMS sites. The automated workflow classifies 14 of the
47 15 known mounds as exploration targets of either high- or medium-priority. This reduces the
48 exploration area to less than 7% of the original survey area from 49 km² to 3.1 km².

49

50 **Keywords:** Convolution Neural Networks, Seafloor Massive Sulfides, Bathymetry, Magnetic
51 Anomaly, CSEM

52

53 **Data Availability Statement:**

54 The bathymetry data used for training the U-Net model are available on open-access repositories as
55 listed in Tab. A1. The AUV-bathymetry and magnetic anomaly maps are available from Peterson
56 (2019) (<https://doi.pangaea.de/10.1594/PANGAEA.899415>) and CSEM data from Gehrman (2019) (
57 <https://doi.pangaea.de/10.1594/PANGAEA.899073>).

58 1 Introduction

59 Over 700 active, inactive and extinct hydrothermal venting sites (cf. definitions in Jamieson &
60 Gartman, 2020) are known to exist along mid-ocean ridges, volcanic arcs, or back-arc spreading
61 centers (Beaulieu et al. 2015; Beaulieu & Szafranski, 2020). Their existence is documented through
62 hydrothermal plumes that are visually confirmed using a suite of underwater-vehicles (e.g., Murton et
63 al., 2019), towed-camera systems (Beaulieu et al., 2013), or via in-situ probing such as gravity coring
64 (Petersen et al., 2016) or seafloor drilling (e.g., Murton et al. 2019). Understanding the distributions of
65 hydrothermal venting, often associated with the evolution of seafloor massive sulfides (SMS), remains
66 a prevalent research topic motivated by the increased demand of strategic minerals needed to foster the
67 net-zero energy transition. The economic and environmental challenges of modern society interfaces
68 with various fields of marine research to predict where subsurface processes transport mineral-
69 enriched, high-temperature fluids from the deep lithosphere towards the seafloor. In many cases these
70 processes are associated with mineral accumulations that form distinct mound-like expressions (e.g.,
71 Fouquet et al. 2010) often referred to as SMS mounds. Current estimates suggest that the abundance of
72 known SMS can contribute a fractional supply of strategic metals in the future (Hannington et al.,
73 2011), albeit the known uncertainties with respect to size, distribution, volume, as well as the
74 environmental impact that would succeed mining these potential deep-sea resources.

75

76 Tonnage estimates of marine minerals are interpreted from seafloor morphology (e.g. Fouquet et al.
77 2010; Graber et al. 2020), geophysical analyses (Haroon et al. 2018; Gehrman et al. 2019; Murton et
78 al. 2019; Galley et al. 2021), or global extrapolations from deposit occurrences along spreading centers
79 (Hannington et al. 2011). Many studies have focused on previously known SMS sites and their
80 immediate surroundings (e.g. Jamieson et al. 2014; Murton et al. 2019; Graber et al. 2020), likely
81 leading to an underestimation of mapped SMS edifices within a given region. For example, Jamieson et
82 al. (2014) discovered over 400 undocumented SMS edifices through manual analysis of high-resolution
83 bathymetry data along the Endeavour Segment. These findings highlight the prevalent question of
84 *where to sample next and in which spatial resolution?* A question often guided by experience, funding,
85 technological constraints and ship-time availability. Moreover, marine scientists recognize the
86 challenges of differentiating prospective SMS mounds from morphologically comparable volcanic
87 constructions (Jamieson et al. 2014) based on bathymetry data alone. In such cases, multivariate
88 databases that include geophysical, geochemical, and geological data acquired across disparate spatial
89 scales can help to 1) identify regions of interest for more detailed in-situ sampling or visual
90 confirmation studies, 2) optimize the use of ship-time through targeted, pre-informed surveying and 3)

91 improve volumetric estimates of SMS candidates via integrative geophysical analyses. However, to
92 process, analyze and interpret this mass of information, integrative data workflows are pivotal for
93 extracting valuable information optimally, improving decision-making tools for localized sampling, and
94 providing more rigorous estimates of known SMS provinces. Here, machine learning (ML) offers
95 avenues to develop coherent data workflows and processing chains sufficiently generic and thereby
96 transferable across various geological domains and data layers. We demonstrate an ML application
97 together with conventional geophysical analyses to automatically detect mound-like morphology on the
98 seafloor and identify distinct high-interest areas based on auxiliary geological and geophysical
99 information to characterize and quantify mineral-enriched SMS targets.

100

101 Geoscientific studies utilizing ML are progressively increasing in environmental and exploration
102 research (e.g., Bouwer et al. 2022; Koedel et al. 2022). ML applications differ not only in the type and
103 spatial and temporal resolution of the input data, but also in the applied techniques. In marine mineral
104 research, ML applications have applied random forest classification (e.g. Gazis et al., 2018) or neural
105 networks (e.g. Keohane & White, 2022; Juliani & Juliani, 2021), focusing mainly on one or two types
106 of input layers (e.g. seafloor images and/or bathymetry data). However, as interdisciplinary SMS
107 databases grow via contributions from geological, geophysical (e.g. Müller, Schwalenberg,
108 Barckhausen, 2023), biological and geochemical applications, ML workflows are expected to also
109 evolve into more generic implementations to facilitate this growing demand of interdisciplinary marine
110 research.

111

112 Our study leverages existing ML applications previously conducted in the marine environment. We
113 introduce a workflow that integrates concurrent data acquired at different spatial scales to better
114 describe the mineral potential within the Trans-Atlantic Geo-traverse (TAG) hydrothermal field. First, a
115 modified approach adapted from Juliani & Juliani (2021) is utilized to identify mound structures in
116 bathymetry data using a U-Net convolutional neural network. Subsequently, the identified mounds are
117 amalgamated with multivariate geophysical and geological databases to assess potential SMS edifices
118 in greater detail. We test the developed workflow using data described in Petersen et al. (2016) and
119 Murton et al. (2018) during two Blue Mining expeditions (<https://blueminig.eu/>) at the TAG
120 hydrothermal field, and compare the results to manual classification studies of Graber et al. (2020) and
121 Murton et al. (2019). This study extends previously published concepts of marine mineral research,
122 which in most cases use a uni-variate database, by including more diversified, multivariate input layers

123 such as reduced-to-the-pole (RTP) magnetics, controlled source and transient electromagnetics (CSEM
124 and TEM), core and grab samples all acquired across various spatial scales.

125

126 **2 Geological and Geophysical Data**

127 The data used in this study were previously published in scientific literature, i.e. Petersen et al. (2016);
128 Murton et al. (2018); Szitkar et al. (2019); Haroon et al. (2018); Gehrman et al., (2019); Graber et al.
129 (2020); Gehrman et al. (2020); Galley et al. (2021). The following describes relevant aspects of the
130 data, which is needed in the context of the ML implementation. Please refer to the above-mentioned
131 literature for more details on data acquisition and geological/geophysical interpretations. It is important
132 to note that from a data science perspective, the available data introduce *a-priori* bias, as these were
133 acquired with the specific purpose of imaging certain physical parameters that, from a geological
134 perspective, are associated with the evolution of SMS. Thus, unknown correlations that extend beyond
135 the current geological understanding of SMS evolution are likely neglected in the presented ML
136 workflow.

137

138 **2.1 Bathymetry Data**

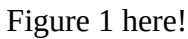
139 Seafloors host numerous focused fluid discharge sites that can appear as mounded manifestations in the
140 seafloor topology (Olakunle et al., 2021). Linking these manifestations to either a volcanic or
141 hydrothermal origin and deriving their potential for forming metalliferous accumulations requires
142 auxiliary data acquired at each specific site. The high-resolution seafloor bathymetry data provides a
143 spatial baseline of where to sample for potential SMS occurrences and also the structural framework
144 for volumetric predictions (e.g., Jamieson et al., 2014; Graber et al., 2020).

145

146 The high-resolution bathymetry data interpreted and classified by the U-Net were collected during
147 research cruise M127 (RV Meteor, 2016) using ship-based multibeam (Fig. 1a) and GEOMAR's
148 Autonomous-Underwater Vehicle (AUV) Abyss (Petersen et al., 2016). Data were acquired using a
149 RESON Seabat 7125 multibeam echosounder, navigated at a speed of three knots using a frequency of
150 200 kHz. The line spacing between adjacent profiles was between 80 m and 100 m at an average
151 altitude of 84 m relative to the seafloor, resulting in a 2 m grid resolution (Fig. 1b). The bathymetry
152 data were processed using the software package MB Systems ([https://www.mbari.org/technology/mb-
153 system/](https://www.mbari.org/technology/mb-system/)) and georeferenced based on prominent seafloor features (Graber et al. (2020) and Szitkar et al.
154 (2019)). This high-resolution bathymetry constructs the baseline of positioning morphological
155 structures during automated segmentation.

156

157 To further optimize the U-Net model, we utilize available high-resolution AUV bathymetry data
158 acquired at different SMS sites around the globe (e.g. Clague et al., 2015; Escartin & Petersen, 2017)
159 and other openly-available bathymetry data. All of the applied bathymetry grids utilized to train,
160 validate and test the U-Net are listed in Tab. A1.

161  Figure 1 here!

162

163 ***2.2 AUV-Based Magnetic Data***

164 The magnetic properties of seafloor basalts are dictated by two alteration processes, namely deuteritic
165 oxidation during the initial cooling phase and the superimposed regional hydrothermal alteration that
166 occurs at younger ages (Ade-Hall et al. 1971). During the latter process, high-temperature fluids can
167 cause permanent demagnetization of basalt due to the alteration of titanomagnetite (Szitkar et al. 2020).
168 Thus, RTP magnetic lows constitute an exploration criterion for the recognition of high-intensity
169 hydrothermal discharge zones and potential SMS deposits in the TAG region (Rona, 1978; Rona,
170 1980). They constitute a meaningful geophysical indicator to differentiate between mounds of
171 hydrothermal and volcanic origin within the TAG hydrothermal field.

172

173 During M127, AUV Abyss was augmented by an Applied Physics System (APS) 1540 Digital three-
174 axis miniature Fluxgate-magnetometer recording at 10 Hz. At the time of the cruise, the Earth's
175 inducing field vector had an inclination of 42° , declination of -15° , and field strength of about 38290
176 nT (Galley et al., 2021). Induced and permanent magnetization effects caused by the AUV itself were
177 removed from the magnetic data by conducting figure-eight calibration dives to solve for the AUV's
178 magnetic properties following Honsho et al. (2013). The magnetic data illustrated in Fig. 2a have been
179 interpreted regionally by Sitkar et al. (2019) and locally around the TAG mound by Galley et al.
180 (2021), and are openly available as a 10 m raster (Petersen, 2019).

181

182 AUV drift relative to the bathymetry leads to indeterminate errors that may propagate into the
183 workflow. Using an inertial system, the AUV's lateral position is tracked from the initially calibrated
184 position. However, water column currents may induce gradual shifts away from the inferred position.
185 In comparison to the vertical position of the AUV that is determined through altimeter and depth
186 readings, a lateral shift between the magnetic anomalies and bathymetric features can either be geology
187 driven (cf. Sitkar et al., 2019) or, alternatively, result from positioning errors; both are relevant

188 constraints for the data integration process of the described ML workflow and are addressed in section
189 3.3.

190 Figure 2 here!

191

192 **2.3 Electrical Conductivity**

193 Accumulations of SMS exhibit a distinct contrast in the electrical resistivity compared to the
194 surrounding basalt (Morgan, 2012; Spagnoli et al., 2016). Sulfide mounds are generally more porous
195 compared to the background basalt (Murton et al., 2019), host high-temperature fluids when active, and
196 contain metalliferous minerals and clays, all attributes that contribute to a decrease of the electrical
197 resistivity. Several electromagnetic applications have been proposed to detect and characterize volumes
198 of minerals for example at TAG (Haroon et al., 2018; Gehrmann et al., 2019) or in the Okinawa
199 Trough (Constable et al., 2018; Ishizu et al., 2019; MacGregor et al., 2021).

200

201 **2.3.1 Controlled Source Electromagnetic Measurements**

202 Our controlled source electromagnetic (CSEM) data were acquired using two, fixed-offset Vulcan
203 receivers (Constable et al. 2016) towed at distances of 350 m and 505 m behind a 50-m horizontal
204 electric dipole (HED) source (Sinha et al., 1990). The resulting 2D resistivity models computed with
205 MARE2DEM (Key, 2016) are interpreted and discussed by Haroon et al. (2018) and Gehrmann et al.
206 (2019, 2020). In summary, the CSEM conductivity models highlight distinct regions of known SMS
207 through increased electrical conductivity (cf. Fig. 3a). Here, we use the acquired CSEM data to reassess
208 the electrical resistivity distributions at identified high-priority sites. Electrical conductance illustrated
209 along CSEM profiles qualitatively define spatial extents of conductive, possibly mineral-enriched
210 seafloor, and predict if morphological expressions are associated with hydrothermal (conductive) or
211 volcanogenic (resistive) activity. Notably, Gehrmann et al. (2020) demonstrate that navigational
212 uncertainty of the CSEM system is not trivial in such complex bathymetry, which can result in
213 inversion artifacts. The authors mitigate these artifacts by estimating the data quality on navigational
214 uncertainties such as instrument position with respect to the bathymetry. Here, we further reduce
215 potential inversion artifacts by confining CSEM inversion models to distinct regions associated with
216 mounds, mitigating potential misinterpretations caused by over-fitting the data at irrelevant locations.

217

218 **2.3.2 Transient Electromagnetic Measurements**

219 Marine transient electromagnetic (TEM) data were acquired at two specific sites within the TAG
220 hydrothermal field using GEOMAR's MARTEMIS system (Fig. 3b and 3c). This coincident loop

221 system consists of one transmitter and one receiver loop, which are housed in a $6.3 \times 6.3 \text{ m}^2$ frame. In
222 regions where seafloor conductivity exceeds the water column conductivity, TEM data will exhibit an
223 increased induced voltage allowing a localized inference of SMS distributions. The system is towed at
224 $<1 \text{ kn}$ and 5 – 15 m above the seafloor and records the electromagnetic response of a 50% duty-cycle
225 transmitter signal at 10 kHz. The acquired time series are processed considering the distorting effects
226 described by Reeck et al. (2020) and transformed into full-space apparent conductivity curves
227 following Eq. 1 of Haroon et al. (2018). Regions of increased apparent conductivity are generally
228 associated with areas where the seafloor is more conductive than the water column resistivity ($\rho < 0.3$
229 Ωm), which in our geological setting is indicative of SMS occurrences (Swidinsky et al. 2012).
230 MARTEMIS positioning was computed through an ultra-short baseline (USBL) transponder attached to
231 the tow cable and merged with the processed apparent conductivity data. The spacing between adjacent
232 stations is approximately 10 m (Fig. 3b and 3c).

233 Figure 3 here!

234

235 **2.4 In-situ Data**

236 Overall, 33 gravity cores of max. 3-m length were acquired within the TAG hydrothermal region during
237 the M127 cruise (Petersen et al., 2016). Locations of possible coring sites were selected with the help
238 of the high-resolution AUV bathymetry data. Twenty-three cores contained abundant sediment, eight
239 contained only fragments of gravel, basalt and traces of sediments in the core catcher, and two were
240 empty (Fig. 3, white markers). Among the 23 sediment cores, 10 had visible hydrothermally-influenced
241 indications (Fig. 3, green triangles); the other cores had the visual appearance of background sediments
242 (carbonate ooze) or showed layers of volcanic origin (Fig. 3, red and blue triangles, respectively). Note
243 that the presence of background sediment or empty cores does not rule out hydrothermal activity at
244 greater depth, as penetration of this coring technique was limited to a maximum of three meters.

245

246 In addition to gravity cores, rock drill samples have been drilled to a maximum depth of 12.5 m below
247 seafloor (Murton et al., 2019). The obtained samples from the Southern, Rona and MIR mounds show
248 high concentrations of minerals, confirming the hydrothermal origin of these three mounds. Here, we
249 link core sites indicative of hydrothermal alteration with collocated EM resistivity data and models to
250 distinguish spatial extents of mineral zones on these mounds and reassess tonnage estimates.

251

252

253

254 **3 Methods**

255 The workflow is split into four steps as illustrated in Fig. 4: 1) selecting and preparing suitable mid-
256 ocean ridge (MOR) bathymetry data, e.g. from accessible open-source data repositories (Tab. A1), 2)
257 training, validating and testing the U-Net model, 3) post-processing of the model output to derive
258 mound architectures and integrate with concurrent RTP magnetic data, and 4) classification and
259 geophysical analysis of identified mounds. The workflow is scripted in Python (Ver. 3.8.12) and uses
260 the Tensorflow (Ver. 2.4.1) library for machine learning tools.

261 

262

263 **3.1. Data Preparation: Bathymetry Data**

264 Bathymetry data used for training are identified as suitable, if a large spatial coverage is acquired at
265 either MORs or at specific hydrothermal fields. Bathymetry rasters are subdivided into overlapping
266 patches of 256 x 256 pixels with a step length of 128 pixels. These pixels are manually annotated using
267 a binary representation, where pixels associated with mounds are labeled as *True* and all other pixels
268 are labeled as *False*. In total, 1899 mounds were manually annotated using the bathymetry data listed in
269 Tab. A1.

270

271 To appear in a common standard that highlights rounded convex and concave morphology through
272 distinct representations, we use a multi-directional slope analysis by mapping the normalized aspect,
273 slope, and the ∂y derivative onto Red, Green and Blue channels of a standardized RGB image,
274 respectively (Fig. 5). The chosen approach converting certain derivatives of bathymetry data into single
275 RGB images facilitates a generalized visual interpretation and aids the model performance. All
276 resulting images show the north flank of mounds in yellow to green moving west to east. Southern
277 mound flanks appear white to blue. Concave features such as pits appear in a reversed manner.

278

279 Note that directional dependencies of background features in the preprocessed images remain unaltered
280 through pre-processing (Figure 5). To increase the amount of training data and mitigate learning of
281 directional dependencies in various settings, input bathymetry was augmented by means of a 90°
282 rotation. As mound structures are near-circular structures, they remain rotational invariant although
283 background strike differs (cf. Fig. 5a and b). In total, 2280 RGB images were produced to train,
284 validate and test the U-Net model, each consisting of 65,536 pixels.

285 

286

287 **3.2 U-Net Implementation, Training and Evaluation**

288 The model architecture yields an end-to-end trainable neural network including segmentation of input
289 images into partitioned pixel sets of corresponding classes. This type of network was first introduced
290 for biomedical image segmentation by Ronneberger et al. (2015) and resembles a symmetric “U” (Fig.
291 6). In our specific case, the U-Net model distinguishes mound from background features and provides
292 values of probabilities (Hu et al., 2015) as outputs.

293

294 For training and testing, only images with at least two percent of the pixels annotated as mounds were
295 considered. Of these, 75 percent were used for training, 20 percent for validation and 5 percent for
296 testing. We use the binary cross entropy loss function defined as:

$$297 \quad H_p(q) = \frac{1}{N} \sum_{i=1}^N y_i \cdot \log(p(y_i)) + (1 - y_i) \log(1 - p(y_i)) \quad (1)$$

298 where y_i refers to the corresponding binary label of each pixel and $p(y_i)$ to the predicted value between
299 0 and 1 within each Epoch i of training. The accuracy, true positive and false negative metrics were
300 computed to determine a point of early stopping, i.e. a model with sufficient accuracy and minimal
301 over-fitting (Fig. 7). The model outputs are contoured at values of >0.5 to outline lateral mound
302 dimensions of the mound pedestal.

303

304 After training, the pre-processed AUV bathymetry image from the TAG area (Petersen, 2016) is
305 presented to the U-Net model as overlapping patches of 256 x 256 pixels. The image reconstruction
306 process is illustrated in Fig. 8. To prevent inaccurate predictions along the image edges, an image
307 smoothing considers only the central 128 x 128 pixels. The outer edges of each predicted patch are
308 neglected. Using an overlapping process, each pixel of the bathymetry grid is included four times
309 within the output prediction. The maximum probability from the four predictions is used as the final
310 pixel probability.

311

312 **3.3. Post-processing of mound structures**

313 The output mound contours define the location and lateral footprints of each mound, which is
314 calculated (in m^2). A minimum threshold of $\sim 1040 m^2$ mound footprint (290 pixels) is introduced to
315 remove most of the falsely detected mound structures caused by geological noise and to focus the
316 analysis on potentially significant SMS volumes (cf. Murton et al. (2019) for discussion). From each of
317 the mound contours, we compute the lateral footprint, maximum height, and median slope using only

318 pixels located within each mound contour. These parameters are used to describe the general mound
319 architecture and are used as inputs for classification.

320

321 For integrating the magnetic anomaly data with the detected mounds from the UNet, an image overlay
322 of gray-scaled hill shade and a diverging red-to-blue magnetic anomaly map (Fig. 2) is cropped and
323 centered around each mound contour, including also peripheral areas. Using the specific red-blue color
324 representation, RTP anomalies appear either red (if positive) or blue (if negative), both being primary
325 color channels within an RGB color spectrum. Color histograms and correlations of the three RGB
326 channels depict positive, negative or a mixture of RTP anomalies into three single values, depending on
327 whether the image is blue, red, or a blue/red blend. The channel correlations serve as inputs for the
328 subsequent classification of the mounds.

329

330 **3.4. Classification & Evaluation**

331 We applied spectral clustering using the Sci-Kit Learn Python Library on the derived parameters for
332 each mound contour. Where available, we added peripheral SMS indicators derived from gravity cores,
333 electromagnetic data and known SMS edifices to determine mound evolution and assess the mineral
334 potential at confirmed high-priority sites. This ensemble of derived morphological expressions and
335 geological/geophysical characteristics was integrated into a new model for the formation of SMS
336 mounds in the TAG hydrothermal field. Further, it provides the basis to re-discuss the resource
337 potential of the field.

338

339 **4 Results**

340 *U-Net analysis*

341 The U-Net metrics indicate an optimal point of early stopping at around Epoch 158 (Fig. 7) . There, the
342 network reached a prediction accuracy of greater than 98.6 and 97.8 percent in training and validation,
343 respectively. The training loss reached 0.032 and the validation loss 0.075 (green and black curves,
344 respectively, in Fig. 7a) using a learning rate of 10^{-4} . A learning trend is observable in the ensuing
345 epochs especially within the training data. Yet, the trend is less pronounced within the validation data,
346 indicating that predictions will not improve for unseen images. To analyze the efficiency of the model,
347 accuracy, true positives and false negatives are also utilized to understand the general characteristics of
348 U-Net predictions (Fig. 7 b-d and Tab. 1).

349

350 Manually annotated mound structures make up, on average, less than 8.2 and 9.1 percent of the total
 351 pixels in each of the training and validation images, respectively. This significant imbalance compared
 352 to background leads to a high starting accuracy of approximately 91 percent, assuming that all pixels
 353 are predicted as background, i.e. *False*. Other metrics, such as true positives and false negatives are
 354 more significant for such imbalanced problems. At the point of early stopping, the trained network can
 355 retrieve 87 percent of the true positive pixels in the validation data, meaning that manually classified
 356 mound pixels are also classified as mound affiliated pixels by the U-Net. Similarly, false negatives are
 357 minimized to less than 1 percent of the total pixels per image during training and validation, indicating
 358 only few background formations are being falsely classified as mounds.

359
 360 In addition to these training metrics, 114 images were used as a test dataset to further assess the U-
 361 Net’s efficiency and prediction characteristics for unseen data. A summary of the test data metrics is
 362 listed in Tab. 1. A prediction accuracy of >97.6 percent is achieved for the test data. Model efficiency
 363 in predicting true positives and avoiding false negatives is comparable to the validation data. Note that
 364 there is some bias to consider in the evaluation of these pixel-based metrics. Discrepancies in mound
 365 dimensions between manual annotation and automated segmentation will reduce model performance,
 366 although a mound is essentially detected by the network. In the majority of studied cases within the test
 367 data, mounds were detected and metric deficiencies arise from discrepancies in lateral mound
 368 extensions between manual and automated annotation (see Fig. S1 of supplementary materials).

Table 1: Metrics and corresponding benchmarks of the applied U-Net model for training, validation and testing images.

Metric	Training		Validation		Test	
Accuracy	<i>Benchmark: 0.91603</i> <i>Prediction: 0.98696</i>		<i>Benchmark: 0.9103</i> <i>Prediction: 0.97790</i>		<i>Benchmark: 0.89777</i> <i>Prediction: 0.976976</i>	
True Positives	<i>Benchmark: 0.08397</i> <i>Prediction: 0.07659</i>	91.2%	<i>Benchmark: 0.08970</i> <i>Prediction: 0.07816</i>	87.1%	<i>Benchmark: 0.10223</i> <i>Prediction: 0.088996</i>	87.1%
False Negatives	<i>Prediction: 0.00738</i>		<i>Prediction: 0.01154</i>		<i>Prediction: 0.01323</i>	

369
 370 The trained U-Net detects a total of 323 mounds within the mapped 49 km² of the AUV bathymetry
 371 data (Fig. 9), each with a lateral footprint greater than 1040 m² (= 290 pixel). The predictions include
 372 all previously identified SMS mounds (cf. Fig.1 and Fig. 9). The lateral mound dimensions match, in
 373 most cases, the manual annotation. However, the U-Net model underestimates the spatial footprint for
 374 Southern and Double Mound. Both mounds show a tectonized surface texture, deviating from an
 375 idealized mound shape, which may explain the reduced model performance. The total number of

376 known mounds accumulates to 16 (compared to 15 of Gehrman et al. 2019) because Double Mound is
 377 segmented as two individual peaks by the U-Net classification.

378

379 The output mounds can be classified into three distinct clusters (Fig. 9) using the elbow method applied
 380 during spectral clustering (K-means). Table 2 lists some statistics for each cluster, including the
 381 minimum, maximum, and mean mound dimensions. The number of associated known SMS sites
 382 defines the priority of each cluster to host SMS. Cluster 1 is assigned a ‘high’ priority, as 10 out of 98
 383 mounds are known to host SMS. A ‘low’ SMS priority is assigned to cluster 3 (1 known SMS site out
 384 of 114 mounds), and ‘medium’ to cluster 2 (4 known SMS sites out of 111 mounds).

Table 2: Clustering statistics of output mounds, including the total area of all mounds and associated mound dimensions. The number of known SMS sites associated with each cluster defines the SMS priority of the cluster.

Cluster # (SMS priority)	Number of Mounds	Number of known SMS sites per Cluster	Total Area of all Mounds	Footprint	Height
1 (high)	98	10	982314 m ²	Max: 141310 m ² Min: 1052 m ² Mean: 10024 m ²	Max: 58.62 m Min: 1.35 m Mean: 14.46 m
2 (medium)	111	4	1188213 m ²	Max: 78268 m ² Min: 1205 m ² Mean: 10704 m ²	Max: 52.53 m Min: 0.35 m Mean: 14.98 m
3 (low)	114	1	942423 m ²	Max: 75269 m ² Min: 1094 m ² Mean: 8266 m ²	Max: 56.34 m Min: 1.12 m Mean: 13.62 m
Total	323	15	3112950 m ²		

385

386 The clustering is primarily driven by the magnetic anomaly data (cf. Fig. S2 and S3); therefore, 10 of
 387 the 15 known SMS sites fall in Cluster 1, showing a distinct negative magnetic anomaly. At these 10
 388 mounds, Szitkar et al. (2019) interprets the magnetic anomalies to represent a vertical hydrothermal
 389 conduit centered above their corresponding source. Known SMS sites of Cluster 2 (4) show both
 390 positive and negative RTP magnetic anomalies indicating either geological alteration or poor AUV
 391 navigation. Cluster 3 contains only one previously known SMS site (Mound #24 from Graber et al.
 392 2020) that is associated with a positive magnetic anomaly. Images of all clustered mounds are
 393 displayed in Fig. S2 of the supplementary materials.

394

395 Despite their magnetic signature, mound morphology is similar in all clusters with respect to their mean
396 heights and mound footprints (cf. Tab. 2 and Fig. S3 in the supplementary materials). Other
397 morphological features indicative of hydrothermal activity, such as jagged contours and number of
398 peaks (Jamieson et al. 2014), could not be identified by our workflow as important parameters for
399 differentiating mound evolution in the TAG area. This leaves the magnetic anomaly as the strongest
400 spatial indicator in the available data set.

401

402 *Spatial Distribution of Morphological Features and Magnetic Footprint*

403

404 The high-priority sites (Cluster 1) occur spatially confined in three bands (labeled Southern, Central
405 and Northern Band in Fig. 9). All bands strike NW-SE, roughly perpendicular to the axis of the Mid-
406 Atlantic Ridge, and coincide well with interfaces between different structural domains identified by
407 Graber et al. (2020). The southern band lies within a region of oblique faults and fissures (Fig. 8 of
408 Graber et al. 2020), that have been suggested to promote upward migration of hot fluids at TAG and
409 other regions (Anderson et al. 2015). The central band of mounds is located within the NW-SE
410 extension of the, so-called, Three-mound area (cf. Graber et al., 2020), runs parallel to mapped
411 corrugations, and connects the Three-Mound regions to the MIR zone (Fig. 9). The northern band lies
412 north of a zone with chaotic seafloor morphology and positive magnetic signature, separating the
413 smooth bathymetry and negative anomalies of the central and northern bands.

414

415 The alignment of Cluster 1 mounds is interrupted in several locations. In the southern band, at around
416 26.138°N and 44.837°W, Cluster 1 mounds are not associated with oblique fissures mapped by (Graber
417 et al. 2020). Instead, negative magnetic anomalies correlate with ‘fresh’ pillow mounds. Such
418 potentially younger magmatic features may mask the oblique fissures typical for the southern band.
419 The northern band contains only one known hydrothermal site named Shimmering, but multiple gravity
420 cores indicate an abundance of hydrothermally-altered sediments in the area (cf. Fig. 9). However,
421 mounds located at the western section of the northern band are structurally interpreted as pillow
422 mounds (Graber et al. 2020).

423

424 *Analysis using Electromagnetic Data*

425 SMS potentials have often assumed homogeneously distributed metal grades across a mounds
426 morphological footprint and its corresponding stockwork zone. Although tonnage estimates are often
427 based on in-situ measurements (i.e. core-log data/seafloor drilling), derived mineral potentials are

428 likely too optimistic because in-situ data are 1) available at only few representative mounds, 2)
429 generally obtained at the points of highest interest, i.e. where SMS is apparent in seafloor imagery and
430 3) penetrate only few meters into the subsurface. In the majority of cases, the structural heterogeneity
431 of individual mounds is either neglected or considered too simplistic, assuming that SMS with high
432 metal grades are distributed across the entire lateral extent of each mound. To constrain this rather
433 generalized assumption, resistivity models derived from CSEM or TEM data appear more suitable to
434 understand the degree of mineralization away from the point-scale core-log data.

435

436 Here, we focus on the electromagnetic data acquired only along high-priority mounds (Cluster 1) or
437 verified mounds that have been documented in preceding literature. CSEM resistivity models that were
438 recomputed for Cluster 1 mounds are illustrated in Fig. 10 using data acquired by Gerhmann et al.
439 (2019). Note that only those mounds are considered that are intersected by CSEM transects. Regions of
440 low resistivity are illustrated by red to orange coloring, background resistivity through green and blue
441 coloring.

442

443 The CSEM resistivity models illustrate that the majority of investigated Cluster 1 mounds are
444 associated with a distinct low-resistivity anomaly of variable magnitude. This, together with core-log
445 data and grab samples (Peterson et al. (2016); Murton et al. (2019)) confirms a certain degree of
446 mineralization at each of the prospective sites. It needs to be noted that in a few instances, i.e. Fig. 10d
447 and 10g, CSEM data has only limited resolution due to the large vertical offset between measurement
448 system (denoted by black markers) and seafloor, thus, limiting a quantitative analysis of mineral grades
449 using CSEM data. Laterally, resistivity distributions and amplitudes do indicate a high degree of
450 certainty and illustrate characteristics of mound composition. Shinkai and Southern mounds, residing in
451 the central band (Fig. 10c through 10e) exhibit a relatively homogeneous conductive structure. These
452 two mounds appear as low-resistive anomalies across their entire lateral footprint (cf. apparent
453 conductivity data in Fig. 3b) indicating that previous mineral estimates could be accurate. In contrast,
454 Double (Fig. 10e) and Rona (Fig. 3b) mound exhibit a low resistive anomaly only in the vicinity of
455 their peaks with no notable contrast to the background resistivity at their pedestal. Although, Rockdrill
456 cores of up to 12 m acquired at the peak of Rona confirm high metal concentrations within a sulfide
457 layer (Murton et al., 2019), TEM data indicates that the majority of Rona's volume is of lower
458 economic value due to a missing apparent conductivity anomaly (Fig. 3b).

459

460 MIR mound has the largest spatial footprint of Cluster 1 mounds in the study area (Fig. 10f). Previous
461 predictions based on mound volumes and extrapolated metal grades derived from gravity cores and
462 rock drill data suggest MIR to be the most economical site within the TAG hydrothermal field (Graber
463 et al. 2020). CSEM inversion of MIR illustrated in Fig. 10f shows an irregular distribution of low-
464 resistive zones across the mound transect indicating the presence of mineralized sediments, but not in
465 the quantity suggested by previous studies. The higher resolution TEM data acquired along multiple
466 transects across the MIR mound support this hypothesis (Fig. 3c) contradicting the notion of MIRs high
467 mineral potential. The point-scale gravity core and Rockdrill data (Peterson et al. (2016); Murton et al.
468 (2019)) were acquired in the northwestern region of the MIR contour, where high apparent
469 conductivities exist. Most of the other regions of the mound structure are not associated with a distinct
470 resistivity anomaly, thus, indicating that mineralization is irregularly distributed across MIR and that
471 tonnage predictions for MIR may be significantly overestimated.

472

473 TAG is arguably the most prominent mound in the study area. Multiple geophysical and geological
474 surveys have focused on the internal mound structure, including the Ocean Drilling Program (ODP)
475 Leg 158 experiment (e.g. Humphris et al., 1995). As such, the internal structure of TAG is well
476 constrained and serves as a blueprint for estimating mineral potentials for other mounds, where less
477 knowledge about internal structure and data are available. The CSEM resistivity models of TAG (Fig.
478 10g and 10h) show an E-W and N-S transect crossing the mound, respectively. Unfortunately,
479 navigation during the E-W transect was chosen too conservative with towing altitudes exceeding 100 m
480 above seafloor, which resulted in inadequate resolution for the TAG's resistivity structure. However,
481 the N-S profile (Fig. 10h) is intriguing, as it supports the asymmetric distribution of mineralization
482 presented in previous studies (e.g Galley et al. 2020). Moreover, the CSEM resistivity model indicates
483 that a significant resistivity contrast compared to the background basalt may only exist for the massive
484 pyrite, pyrite-anhydrite, pyrite-silica and possibly the pyrite silica units (see Knott et al. 1998). Hence,
485 the applied CSEM configuration is likely unsuitable for detecting the stockwork structure and requires
486 higher resolution CSEM data acquired in a 3D survey as demonstrated by MacGregor et al. (2021).

487

488 **5 Discussion**

489 ***5.1 Automated SMS Mapping using Machine Learning***

490 The presented workflow can be used as a blueprint for prioritizing SMS exploration targets at mid-
491 ocean ridges and understanding distributions of mineral potentials. The workflow reduces the total area
492 of interest from the surveyed 49 km² to 3.1 km², which in turn can be further reduced to either 1.92 km²

493 (Clusters 1 and 2) or 0.98 km² (only Cluster 1) using additional magnetic constraints (i.e. mounds with
494 magnetic lows). Moreover, the latitudinal bands of hydrothermal activity identified through this
495 integrated analysis reveal prospective areas where to search for SMS and may also exist at other
496 MORs. The workflow is fully automated, allowing us to identify regions of interest in quasi real-time
497 (if a pre-trained model exists) when new data is acquired, thus, reducing exploration costs considerably
498 and permitting more focused surveying. Additionally, the workflow is adaptable to future developments
499 in marine mineral exploration and research and its application in other survey areas with similar or
500 additional data layers appears feasible.

501

502 The data preparation part of our workflow seeks to unify the bathymetry data, acquired at different
503 spatial resolution and at various sites across the globe, into a common representation independent of the
504 actual depth, slope, and curvature within a given area. Juliani & Juliani (2021) propose a principal
505 component analysis (PCA) consisting of both a change in slope and a multi-directional shading of
506 elevation data in order to reduce the bathymetric inputs. However, our analysis shows that PCA may
507 not generalize well for bathymetry data acquired at different regions with variable roughness and
508 geological strike. A key advantage of our proposed processing scheme is notably that bathymetry data
509 from different regions will unify onto a single coherent visualization.

510

511 Moreover, the workflow also allows to test and use other types of ML segmentation tools, and to
512 include additional data layers (e.g. high-resolution backscatter, self-potential, etc). As many of these
513 additional data layers are currently not available in open-access repositories, they can be integrated
514 best within the post-processing step. As backscatter and self-potential data become more readily
515 available, it is also feasible to train the U-Net directly for different types of mound characteristics. The
516 integration of such additional data will likely increase ambiguity, but presumably achieve higher
517 certainty in identifying SMS sites.

518

519 Following Szitkar et al. (2019) and Rona (1978; 1980), hydrothermal mounds within the TAG
520 hydrothermal field are associated with a distinct negative RTP magnetic anomaly, whereas volcanic
521 edifices typically display positive values. This characteristic proves suitable for clustering depicted
522 mound contours into groups to identify their potential origins. However, three aspects must be
523 considered to integrate the magnetic footprint of a mound or a group of adjacent mounds with the
524 corresponding bathymetry attributes.

525

- 526 1. Magnetic anomaly data are acquired at a resolution of 10 m grid spacing compared to the 2 m
527 resolution of the bathymetry data. A pixel-wise comparison between magnetic anomalies and
528 morphological features requires an up-sampling of the magnetic anomaly data, which may lead
529 to interpolation artifacts.
- 530 2. An RTP magnetic anomaly shows magnetization and geomagnetic field vectors that render
531 vertical anomalies above the causative body. However, Szitkar et al. (2019) discuss that tectonic
532 events can tilt the crustal block causing altered shapes of the magnetic anomalies, leading to
533 incoherent magnetic anomalies associated with morphological expression. A similar effect is
534 also observable if tectonic forces act on a previously deposited mound.
- 535 3. AUV magnetic data are susceptible to errors that arise from inaccuracies in AUV positioning
536 relative to its calibrated coordinates. This may lead to a lateral shift between the morphological
537 expression and the corresponding RTP magnetic anomaly.

538

539 All three undetermined circumstances lead to uncertainties in a pixel-wise integration of the magnetic
540 and corresponding bathymetry pixels. Hence, a relaxation of spatial similarities between mound
541 structures and resulting magnetic anomalies is required and was implemented in our analysis.

542

543 The approach would benefit from a greater number of annotated bathymetry data available in online
544 repositories to improve model training. The chosen study area belongs to the most studied
545 hydrothermal sites globally, and, provides a solid first training set. The developed workflow focuses on
546 the analysis of high-resolution bathymetry data, which resemble the most common collected data in
547 seafloor exploration. Given the steady increase of sea-going SMS research, manual assessments of each
548 individual data layer becomes increasingly difficult and automatization of workflows will be inevitable.
549 Therefore, application of the workflow in other hydrothermal areas either at mid-ocean ridges or other
550 geological environments with complex, rough terrain, is a crucial future task.

551

552 ***5.2 Implications for hydrothermal activity in the TAG area***

553 Notably, marine mineral exploration is a complex endeavor unlikely solved by a silver bullet approach.
554 Thus, various ML strategies and conventional geoscientific research will attest a feasibility for
555 detecting SMS and estimating mineral potentials. The proposed ML strategy does not contradict this
556 notion, but instead, offers a means of integrating multivariate data into a common interpretation scheme
557 that is easily audited. Note that the delineation of convex structures in bathymetry data underlies some
558 variability resulting from terrain analysis and, even if conducted manually, remains ambiguous due to

559 interfering geomorphic processes that mask or distort typical mound morphologies. Hence, although
560 mapping the correct mound dimensions is significant for addressing mineral potentials, discrepancies
561 between manual and automated segmentation are expected.

562

563 Despite these explainable deviations, the spatial alignment of Cluster 1 bands is clearly visible and the
564 correlation to structural domains defined by Graber et al. (2020) is apparent. This may support the
565 hypotheses of a structural heterogeneity within the hydrothermal field dictating the distribution of SMS
566 edifices, as proposed by Graber et al. (2020). Both the spatial extent of the alignment and the
567 occurrence of deviating areas indicate a structural constraint in the deep subsurface. This dominant
568 structural constraint supports an interpretation where a strongly distorted subsurface structuring (e.g.
569 bend detachment fault) leads to focused fluid flow in the deep subsurface that results in linear, off-axis,
570 distribution of hydrothermal edifices. Moreover, the various upflow zones are likely to span a region
571 larger than the investigated area of study. Further sites may be located north of Shimmering and also
572 south of TAG, as well as in the westward extension of the three bands. Conclusively, the presented
573 workflow has demonstrated a successful amalgamation of spatially acquired bathymetry and magnetic
574 data, which could be used to inform future AUV bathymetry and magnetic surveying.

575

576 Although the number of potential SMS sites drastically increased through this automated analysis,
577 mineral potential of the TAG hydrothermal field is likely lower than originally presumed.
578 Electromagnetic data illustrates that mineralized zones for the largest proposed SMS sites are generally
579 heterogeneously distributed across the mound contour, thus, contradicting the proposed high tonnage
580 estimates using homogeneously distributed mineral grades derived from point-scale measurements. We
581 propose that future analysis of SMS tonnages should incorporate multiple seafloor drillings conducted
582 across the mound contours with additional data layers (e.g. backscatter, seismics, and 3D CSEM
583 inversion models) to achieve a high degree of certainty in the tonnage estimation. If such high-
584 resolution survey strategy for SMS sites is economical, remains beyond the scope of this study.

585

586 The current SMS priority depends mainly on AUV magnetic data and on the number of known SMS
587 sites within a given cluster. The former is not typically considered a conventional data layer in SMS
588 exploration and should be added to the necessary SMS exploration criteria. Furthermore, it cannot be
589 ruled out that future endeavors may potentially change the presented prioritization of SMS mounds
590 through more SMS discoveries or through the acquisition of additional data layers (e.g. high-resolution
591 backscatter, resistivity or self-potential data). It is expected that not all mounds within the high-priority

592 cluster are associated with SMS edifices and that additional data layers will improve the certainty of the
593 automated SMS prediction. Overall, a more diversified dataset measured at numerous SMS sites across
594 the global MORs will only help improve our understanding of SMS predictors and improve future
595 developments of ML workflows.

596

597 Marine CSEM and TEM data have demonstrated additional value when conducting tonnage estimates
598 for SMS sites. However, more development is required to improve the significance of resistivity
599 models to help quantifying volumes of mineralized zones within a mound edifice. Most notably, high-
600 resolution 3D surveys using AUV technology are likely required to accurately derive spatial extensions
601 of conductive material in these remote settings. MacGregor et al. (2021) have already presented a first
602 3D application and inversion of CSEM data and others are likely to follow suit, given the increased
603 value of electrical resistivity models to constrain volumetric predictions.

604

605 **6 Conclusion**

606 A workflow to conduct automated SMS site detection using multivariate geoscientific data is presented
607 that employs a U-Net neural network to identify prominent mound-like morphologies in bathymetry
608 data. The predicted contours are subsequently integrated with other spatial data layers (e.g. AUV
609 magnetic data) to identify high-priority sites for SMS prospecting. Within the 49 km² grid of high-
610 resolution bathymetry data, 323 mounds were detected. 98 of these were classified as high priority due
611 to their architecture and magnetic signature. Moreover, from the automated analysis 14 (10 high, 4
612 medium) of the 15 known SMS sites in the TAG area were identified as either high or medium priority.
613 Only one known site was classified within the low-priority group. The high-priority sites were spatially
614 distributed into latitudinal bands, supporting the hypotheses that focused fluid-flow at depth leads to
615 linear distributions of off-axis SMS edifices in the area.

616

617 The presented workflow cannot only be used to improve analysis and interpretation of previously
618 surveyed areas, but also serve as a blueprint to optimize SMS exploration at sea. The trained model
619 can be applied on newly acquired bathymetry data in quasi real-time to determine prospective zones for
620 more detailed confirmation/visualization studies. Thus, optimizing the use of ship time and reducing
621 exploration costs. The workflow is very adaptable to include additional data layer such as backscatter,
622 self-potential, turbidity and other water column data maps if available.

623

624 Electrical resistivity models demonstrate that mineralization of SMS mounds are less homogeneous
625 than often considered. Thus, indicating that high-grade mineral contents in SMS are not equally
626 distributed across the entire mound and that tonnage estimates may be significantly overestimated.
627 Consequently, although the workflow detects many more potential SMS edifices than previously
628 known, the overall resource potential of the TAG hydrothermal field is likely lower than previously
629 assumed.

630

631 **7 Acknowledgments**

632 AH was in part funded by the Digital Earth and SMART Projects at GEOMAR Helmholtz Centre of
633 Ocean Research Kiel.

634

635 **8 References**

636 Ade-Hall, J. M., Palmer, H. C. & Hubbard, T. P. (1971). The magnetic and opaque petrological
637 response of basalt to regional hydrothermal alteration. *Geophys. J. R. Astron. Soc.* 24, 137–174.

638

639 Andersen, C., Rüpke, L., Hasenclever, J., Grevemeyer, I., Petersen, S. (2015). Fault geometry and
640 permeability contrast control vent temperatures at the Logatchev 1 hydrothermal field, Mid-
641 Atlantic Ridge. *Geology*, 43 (1): 51–54. doi: <https://doi.org/10.1130/G36113.1>

642

643 Beaulieu, S. E., E. T. Baker, C. R. German, and A. Maffei (2013). An authoritative global database for
644 active submarine hydrothermal vent fields, *Geochem. Geophys. Geosys.*, 14, 4892–4905,
645 <https://doi.org/10.1002/2013GC004998>.

646

647 Beaulieu, S.E., Baker, E.T., German, C.R. (2015). Where are the undiscovered hydrothermal vents on
648 oceanic spreading ridges? *Deep-Sea Research Part II: Topical Studies in Oceanography*, 121,
649 202-212, <https://doi.org/10.1016/j.dsr2.2015.05.001>.

650

651 Beaulieu, S.E., Szafranski, K. (2020). InterRidge Global Database of Active Submarine Hydrothermal
652 Vent Fields, Version 3.4. World Wide Web electronic publication available from [http://vents-](http://vents-data.interridge.org)
653 [data.interridge.org](http://vents-data.interridge.org) Accessed 2022-12-01.

654

655 Bouwer, L. M., Dransch, D., Ruhnke, R., Rechid, D., Frickenhaus, S., & Greinert, J. (2022). Integrating
656 data science and earth science: Challenges and solutions (L. M. Bouwer, D. Dransch, R.
657 Ruhnke, D. Rechid, S. Frickenhaus, & J. Greinert, Eds.). Springer Nature.
658 <https://doi.org/10.1007/978-3-030-99546-1>

659

660 Clague, David, et al., (2015). Processed near-bottom Sidescan Sonar Data (version 2) from the Juan de
661 Fuca Spreading Center - Endeavour Segment acquired with AUV D. Allan B. during the Zephyr
662 expedition ZPR1108 (2011). Interdisciplinary Earth Data Alliance (IEDA),
663 <https://doi.org/10.1594/IEDA/321990>.

664

665 Constable, S., Kannberg, P. K., and Weitemeyer, K. (2016). Vulcan: A deep-towed CSEM receiver,
666 *Geochem. Geophys. Geosyst.*, 17, 1042– 1064, doi:[10.1002/2015GC006174](https://doi.org/10.1002/2015GC006174).

667

668 Constable, S., Kowalczyk, P. and Bloomer, S. (2018). Measuring marine self-potential using an
669 autonomous underwater vehicle, *Geophysical Journal International*, Volume 215, Issue 1,
670 October 2018, Pages 49–60, <https://doi.org/10.1093/gji/ggy263>.

671

672 Escartín J. & Petersen S. (2017). ODEMAR AUV Abyss (GEOMAR) + shipboard Pourquoi Pas?
673 multibeam bathymetry - 13deg20'N and 13deg30'N Oceanic Core Complexes, Mid Atlantic
674 Ridge. SEANO. <https://doi.org/10.17882/48335>.

675

676 Escartin J., Mevel C., Petersen S., Bonnemains D., Cannat M., Andreani M., Augustin N., Bezos A.,
677 Chavagnac V., Choi Y., Godard M., Haaga K., Hamelin C., Ildefonse B., Jamieson J., John B.,
678 Leleu T., Macleod C. J., Massot-Campos M., Nomikou P., Olive J. A., Paquet M., Rommevaux
679 C., Rothenbeck M., Steinfuhrer A., Tominaga M., Triebe L., Campos R., Gracias N., Garcia R.
680 (2017). Tectonic structure, evolution, and the nature of oceanic core complexes and their
681 detachment fault zones (13°20'N and 13°30'N, Mid-Atlantic Ridge). *Geochemistry Geophysics*
682 *Geosystems*, 18(4), 1451-1482. Publisher's official version :
683 <https://doi.org/10.1002/2016GC006775> , Open Access version :
684 <https://archimer.ifremer.fr/doc/00376/48702/>.

685

686 Fouquet, Y., Cambon, P., Etoubleau, J., Charlou, J.L., Ondreas, H., Barriga, F.J.A.S., Cherkashov, G.,
687 Semkova, T., Poroshina, I., Bohn, M., Donval, J.P., Henry, K., Murphy, P., Rouxel, O., (2010).
688 Geodiversity of hydrothermal processes along the Mid-Atlantic Ridge and ultramafic-hosted
689 mineralization: a new type of oceanic Cu-Zn-Co-Au volcanogenic massive sulfide deposit.
690 Article *Geophys. Monogr. Ser.* 188, 321–367.

691

692 Galley, C., Lelièvre, P., Haroon, A., Graber, S., Jamieson, J., Sztikar, F., et al. (2021). Magnetic and
693 gravity surface geometry inverse modeling of the TAG active mound. *Journal of Geophysical*
694 *Research: Solid Earth*, 126, e2021JB022228. <https://doi.org/10.1029/2021JB022228>.

695

696 Gazis, I-Z., Schoening, T., Alevizos, E., Greinert, J. (2018). Quantitative mapping and predictive
697 modeling of Mn nodules' distribution from hydroacoustic and optical AUV data linked by
698 random forests machine learning, *Biogeosciences*, 15, 7347-7377, <https://doi.org/10.5194/bg-15-7347-2018>.

700

701 Gehrmann, R.A.S., Haroon, A., Morton, M., Djanni, A.T., Minshull, T.A. (2020). Seafloor massive
702 sulphide exploration using deep-towed controlled source electromagnetics: navigational
703 uncertainties, *Geophysical Journal International*, Volume 220, Issue 2, Pages 1215–1227,
704 <https://doi.org/10.1093/gji/ggz513>.

705

706 Gehrmann, R., North, L. J., Graber, S., Sztikar, F., Petersen, S., Minshull, T. A., & Murton, B. J. (2019).
707 Marine mineral exploration with controlled source electromagnetics at the TAG hydrothermal
708 field, 26° N Mid-Atlantic Ridge. *Geophysical Research Letters*, 46, 5808–5816.
709 <https://doi.org/10.1029/2019GL082928>.

710

711 Gehrmann, R.A.S. (2019): Controlled-source electromagnetic data from the TAG hydrothermal field,
712 26N Mid-Atlantic Ridge. PANGAEA, <https://doi.org/10.1594/PANGAEA.899073>, Supplement
713 to: Gehrmann, Romina A S; North, Laurence J; Graber, Sebastian; Sztikar, Florent; Petersen, S;
714 Minshull, Tim A; Murton, Bramley J (2019): Marine Mineral Exploration With Controlled

715 Source Electromagnetics at the TAG Hydrothermal Field, 26°N Mid-Atlantic Ridge.
716 Geophysical Research Letters, 46(11), 5808-5816, <https://doi.org/10.1029/2019GL082928>
717

718 Graber, S., Petersen, S., Yeo, I., Sztikar, F., Klischies, M., Jamieson, J., et al. (2020). Structural control,
719 evolution, and accumulation rates of massive sulfides in the TAG hydrothermal field.
720 *Geochemistry, Geophysics, Geosystems*, 21, e2020GC009185.
721 <https://doi.org/10.1029/2020GC009185>.
722

723 Hannington, M., Jamieson, J.W., Monecke, T., Petersen, S., Beaulieu, S. (2011). The abundance of
724 seafloor massive sulfide deposits, *Geology*, 39, 1155-1158, <https://doi.org/10.1130/G32468.1>.
725

726 Haroon, A., Hölz, S., Gehrman, R.A.S., Attias, E., Jegen, M., Minshull, T.A., Murton, B.J. (2018).
727 Marine dipole-dipole controlled source electromagnetic and coincident-loop transient
728 electromagnetic experiments to detect seafloor massive sulphides: effects of three-dimensional
729 bathymetry, *Geophysical Journal International*, Volume 215, Issue 3, Pages 2156–2171,
730 <https://doi.org/10.1093/gji/ggy398>.
731

732 Honsho, C., Ura, T., & Kim, K. (2013). Deep-sea magnetic vector anomalies over the Hakurei
733 hydrothermal field and the Bayonnaise knoll caldera, Izu-Ogasawara arc, Japan. *Journal of*
734 *Geophysical Research: Solid Earth*, 118, 5147–5164. <https://doi.org/10.1002/jgrb.50382>.
735

736 Hu, Fan, Gui-Song Xia, Jingwen Hu, and Liangpei Zhang (2015). Transferring Deep Convolutional
737 Neural Networks for the Scene Classification of High-Resolution Remote Sensing Imagery
738 *Remote Sensing* 7, no. 11: 14680-14707. <https://doi.org/10.3390/rs71114680>.
739

740 Humphris, S. E., Herzig, P. M., Miller, D. J., Alt, J. C., Becker, K., Brown, D., et al. (1995). The
741 internal structure of an active sea-floor massive sulphide deposit. *Nature*, 377(6551), 713–716.
742 <https://doi.org/10.1038/377713a0>
743

744 Hübscher, C., Beier, C. (2022). Multibeam bathymetry processed data (EM 120 echosounder &
745 Kongsberg EM 122 dataset compilation) of RV METEOR during cruise M79/2, M113/1 &
746 M128, Azores Plateau between the Terceira Rift and the East Azores Fracture Zone, North
747 Atlantic Ocean. PANGAEA, <https://doi.org/10.1594/PANGAEA.945528>.
748

749 Ishizu, K., Goto, T., Ohta, Y., Kasaya, T., Iwamoto, H., Vachiratienchai, C., et al. (2019). Internal
750 Structure of a Seafloor Massive Sulfide Deposit by Electrical Resistivity Tomography, Okinawa
751 Trough. *Geophysical Research Letters*, 46, 11025– 11034.
752 <https://doi.org/10.1029/2019GL083749>
753

754 Jamieson, J.W., Clague, D.A., Hannington, M.D. (2014). Hydrothermal sulfide accumulation along the
755 Endeavour Segment, Juan de Fuca Ridge, *Earth and Planetary Science Letters*, 395, 136-148,
756 <http://dx.doi.org/10.1016/j.epsl.2014.03.035>.
757

758 Jamieson, J.W. & Gartman, A. (2020). Defining active, inactive, and extinct seafloor massive sulfide
759 deposits, *Marine Policy*, 117, 103926, <https://doi.org/10.1016/j.marpol.2020.103926>.
760

761 Juliani, C., Juliani, E. (2021). Deep learning of terrain morphology and pattern discovery via network-
762 based representational similarity analysis for deep-sea mineral exploration, *Ore Geology*
763 *Reviews*, 129, 103936, <https://doi.org/10.1016/j.oregeorev.2020.103936>.

764

765 Keohane, I., and White, S. (2022). "Chimney Identification Tool for Automated Detection of
766 Hydrothermal Chimneys from High-Resolution Bathymetry Using Machine Learning"
767 *Geosciences* 12, no. 4: 176. <https://doi.org/10.3390/geosciences12040176>.

768

769 Key, K. (2016). MARE2DEM: a 2-D inversion code for controlled-source electromagnetic and
770 magnetotelluric data, *Geophysical Journal International*, Volume 207, Issue 1, Pages 571–588,
771 <https://doi.org/10.1093/gji/ggw290>

772

773 Knott, R., Fouquet, Y., Honnorez, J., Pertersen, S., Bohn, M. (1998). Petrology of hydrothermal
774 mineralization: A vertical section through the TAG mound. *Proceedings of the Ocean Drilling
775 Program: Scientific Results*, 158, 5-26, <https://doi.org/10.2973/odp.proc.sr.158.201.1998>.

776

777 Koedel, U. *et al.* (2022). The Digital Earth Smart Monitoring Concept and Tools. In: Bouwer, L.M.,
778 Dransch, D., Ruhnke, R., Rechid, D., Frickenhaus, S., Greinert, J. (eds) Integrating Data
779 Science and Earth Science. SpringerBriefs in Earth System Sciences. Springer, Cham.
780 https://doi.org/10.1007/978-3-030-99546-1_6.

781

782 MacGregor, L., Kowalczyk, P., Galley, C., Weitemeyer, K., Bloomer, S., Phillips, N., Proctor, A. (2021).
783 Characterization of Seafloor Mineral Deposits Using Multiphysics Datasets Acquired from an
784 AUV, *First Break*, 39 (8), 63-69, <https://doi.org/10.3997/1365-2397.fb2021062>.

785

786 Morgan, L. A., (2012). Geophysical characteristics of volcanogenic massive sulfide deposits, in
787 Volcanogenic Sulfide Occurrence Model, pp. 115–131, eds ,Pat Shanks W.C., III & Thurston, R.,
788 USGS.

789

790 Murton, B.J. and Shipboard Scientific Party (2018). Cruise Report: Expedition JC138: 29th June-8th
791 August 2016, Mid Atlantic Ridge, 26°8.38'N; 44°49.92'W, National Oceanography Centre
792 Southampton, Southampton, pp. 285.
793 https://www.bodc.ac.uk/resources/inventories/cruise_inventory/reports/jc138.pdf (accessed 29
794 November 2022).

795

796 Murton, B.J., Lehrmann, B., Dutrieux, A. M., Martins, S., Gil de la Iglesia, A., Stobbs, I.J., Barriga,
797 F.J.A.S., Bialas, J., Dannowski, A., Vardy, M.E., North, L.J., Yeo, I.A.L.M., Lusty, P.A.J.,
798 Petersen, S. (2019). Geological fate of seafloor massive sulphides at the TAG hydrothermal
799 field (Mid-Atlantic Ridge), *Ore Geology Reviews*, 107, 903-925,
800 <https://doi.org/10.1016/j.oregeorev.2019.03.005>.

801

802 Müller, H., Schwalenberg, K., Barckhausen, U. (2023). Magnetic and electromagnetic exploration of
803 SMS deposits; perspectives and frontiers, 84th EAGE Annual Conference & Exhibition, Volume
804 2023, p. 1-5, <https://doi.org/10.3997/2214-4609.2023101269>.

805

806 Olakunle, O.K., Ajibola, L.M., Muhammad, I.H. *et al.* (2021). Massive seafloor mounds depict
807 potential for seafloor mineral deposits in the Great South Basin (GSB) offshore New Zealand.
808 *Sci Rep* 11, 9185. <https://doi.org/10.1038/s41598-021-88620-x>.

809

810 Petersen, S. and Shipboard Scientific Party (2016). *RV METEOR Cruise Report M127 Metal fluxes and
811 Resource Potential at the Slow-spreading TAG Midocean Ridge Segment (26°N, MAR) – Blue
812 Mining@Sea, Bridgetown (Barbados) – Ponta Delgada (Portugal), 25.05.-28.06.2016.*

813 GEOMAR Report, N. Ser. 032 . GEOMAR Helmholtz-Zentrum für Ozeanforschung Kiel, Kiel,
814 87, 69 pp. DOI [10.3289/GEOMAR_REP_NS_32_2016](https://doi.org/10.3289/GEOMAR_REP_NS_32_2016).
815

816 Petersen, Sven (2019). Bathymetric data products from AUV dives during METEOR cruise M127
817 (TAG Hydrothermal Field, Atlantic). GEOMAR - Helmholtz Centre for Ocean Research Kiel,
818 PANGAEA, <https://doi.org/10.1594/PANGAEA.899415>.
819

820 Reeck, K., Müller, H., Hölz, S., Haroon, A., Schwalenberg, K. and Jegen, M. (2020). Effects of
821 metallic system components on marine electromagnetic loop data. *Geophysical Prospecting*, 68:
822 2254-2270. <https://doi.org/10.1111/1365-2478.12984>.
823

824 Rona, P. A. (1978). Criteria for recognition of hydrothermal mineral deposits in oceanic crust.
825 *Economic Geology*; 73 (2): 135–160. doi: <https://doi.org/10.2113/gsecongeo.73.2.135>
826

827 Rona, P. A. (1980). TAG hydrothermal Field: Mid-Atlantic Ridge crest at latitude 26°N. Geological
828 Society of London. *Journal* 137, 385–402, <https://doi.org/10.1144/gsjgs.137.4.038>.
829

830 Ronneberger, O., Fischer, P., Brox, T. (2015). U-Net: Convolutional Networks for Biomedical Image
831 Segmentation. In: Navab, N., Hornegger, J., Wells, W., Frangi, A. (eds) *Medical Image*
832 *Computing and Computer-Assisted Intervention – MICCAI 2015*. MICCAI 2015. Lecture
833 Notes in Computer Science(), vol 9351. Springer, Cham. [https://doi.org/10.1007/978-3-319-](https://doi.org/10.1007/978-3-319-24574-4_28)
834 [24574-4_28](https://doi.org/10.1007/978-3-319-24574-4_28).
835

836 Sinha, M.C., Patel, P.D., Unsworth, M.J. *et al.* (1990). An active source electromagnetic sounding
837 system for marine use. *Marine Geophysical Researches* 12, 59–68 .
838 <https://doi.org/10.1007/BF00310563>.
839

840 Spagnoli, G., , Hannington, M., Bairlein, K., Hördt, A., Jegen, M., Petersen , S. & Laurila, T. (2016).
841 Electrical properties of seafloor massive sulfides, *Geo Mar. Lett.*, 36, 235–245.
842

843 Swidinsky, A., Hölz, S. and Jegen, M. (2012). On mapping seafloor mineral deposits with central loop
844 transient electromagnetics, *Geophysics*, 77, 3, E171-E184. [https://doi.org/10.1190/geo2011-](https://doi.org/10.1190/geo2011-0242.1)
845 [0242.1](https://doi.org/10.1190/geo2011-0242.1)
846

847 Szitkar, F., Dymant, J., Petersen, S. *et al.* (2019). Detachment tectonics at Mid-Atlantic Ridge 26°N.
848 *Sci Rep* 9, 11830. <https://doi.org/10.1038/s41598-019-47974-z>.
849

850 Villinger, Heinrich; Strack, Anne; Gaide, Stefanie; Thal, Janis (2018). Gridded bathymetry of North
851 Pond (MAR) from multibeam echosounder EM120 and EM122 data of cruises MSM20/5
852 (2012) and MSM37 (2014). Department of Geosciences, Bremen University, PANGAEA,
853 <https://doi.org/10.1594/PANGAEA.889439>.
854
855
856

Table A1: List of open-access bathymetry data used for training the U-Net.

Index	Extent		Resolution	Source / Reference
	Longitude Min. Longitude Max.	Latitude Min. Latitude Max		
1	-44.99625 -44.69042	25.98625 26.28625	~ 90 m	Multibeam Mosaic https://www.ncei.noaa.gov/maps/bathymetry/
2	-43.23542 -41.31541	29.69375 30.78042	~ 90 m	Multibeam Mosaic https://www.ncei.noaa.gov/maps/bathymetry/
3	-34.45958 -33.12792	35.45792 37.50708	~ 90 m	Multibeam Mosaic https://www.ncei.noaa.gov/maps/bathymetry/
4	-27.14292 -23.76958	61.70625 63.44625	~ 90 m	Multibeam Mosaic https://www.ncei.noaa.gov/maps/bathymetry/
5	-45.21799 -44.40485	25.77404 26.54754	~ 30 m	Petersen (2019) https://doi.org/10.1594/PANGAEA.899415
6	-44.85162 -44.75758	26.10058 26.18684	~ 2 m	Petersen (2019) https://doi.org/10.1594/PANGAEA.899415
7	-44.97116 -44.86794	13.27914 13.34156	~ 2m	Escartin & Petersen (2017) and Escartin et al. (2017)
8	-45.00966 -44.88124	13.48664 13.52226	~ 2 m	Escartin & Petersen (2017) and Escartin et al. (2017)
9	-46.45929 -45.81298	22.36806 23.05779	~ 10 m	Villinger et al. (2018) https://doi.org/10.1594/PANGAEA.889439
10	-34.99333 -31.87833	56.69666 58.00000	~ 90 m	Multibeam Mosaic https://www.ncei.noaa.gov/maps/bathymetry/
11	-42.40119 -41.72925	29.82935 30.36156	~ 90 m	Multibeam Mosaic https://www.ncei.noaa.gov/maps/bathymetry/
12	-129.1490 -129.0070	47.88199 48.08900	~ 1 m	Clague et al. (2015) http://get.iedadata.org/doi/321990
13	-177.1383 -176.3533	-23.0983 -21.5792	~ 90 m	Multibeam Mosaic https://www.ncei.noaa.gov/maps/bathymetry/
14	-29.93012 -22.78952	35.99997 39.50023	~ 45 m	Hübscher & Beier (2022) https://doi.pangaea.de/10.1594/PANGAEA.945528

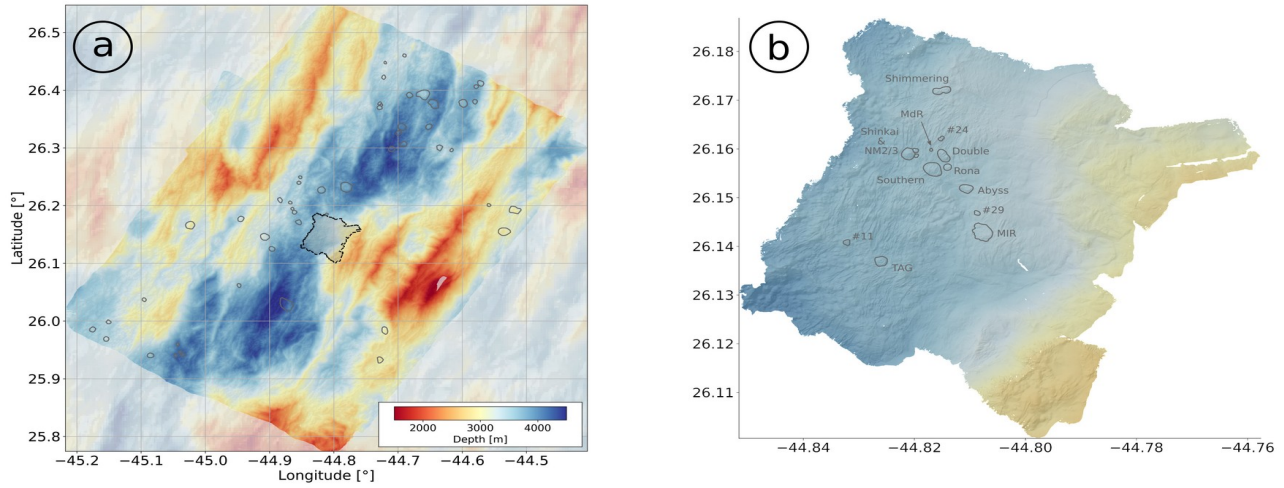


Figure 1: Bathymetry maps of the study area. (a) GEBCO bathymetry (shaded map) overlain by the ship-based bathymetry data acquired during RV Meteor cruise M127 with a spatial resolution of 30 m. Gray outlines denote visible mound structures whereas the black outlined region denotes the high-resolution bathymetry survey illustrated in (b). (b) AUV bathymetry data acquired with a spatial resolution of 2 m using the same color scale as in (a). Known SMS mounds are outlined and labeled as depicted by Graber et al. (2020).

859 |
860 |

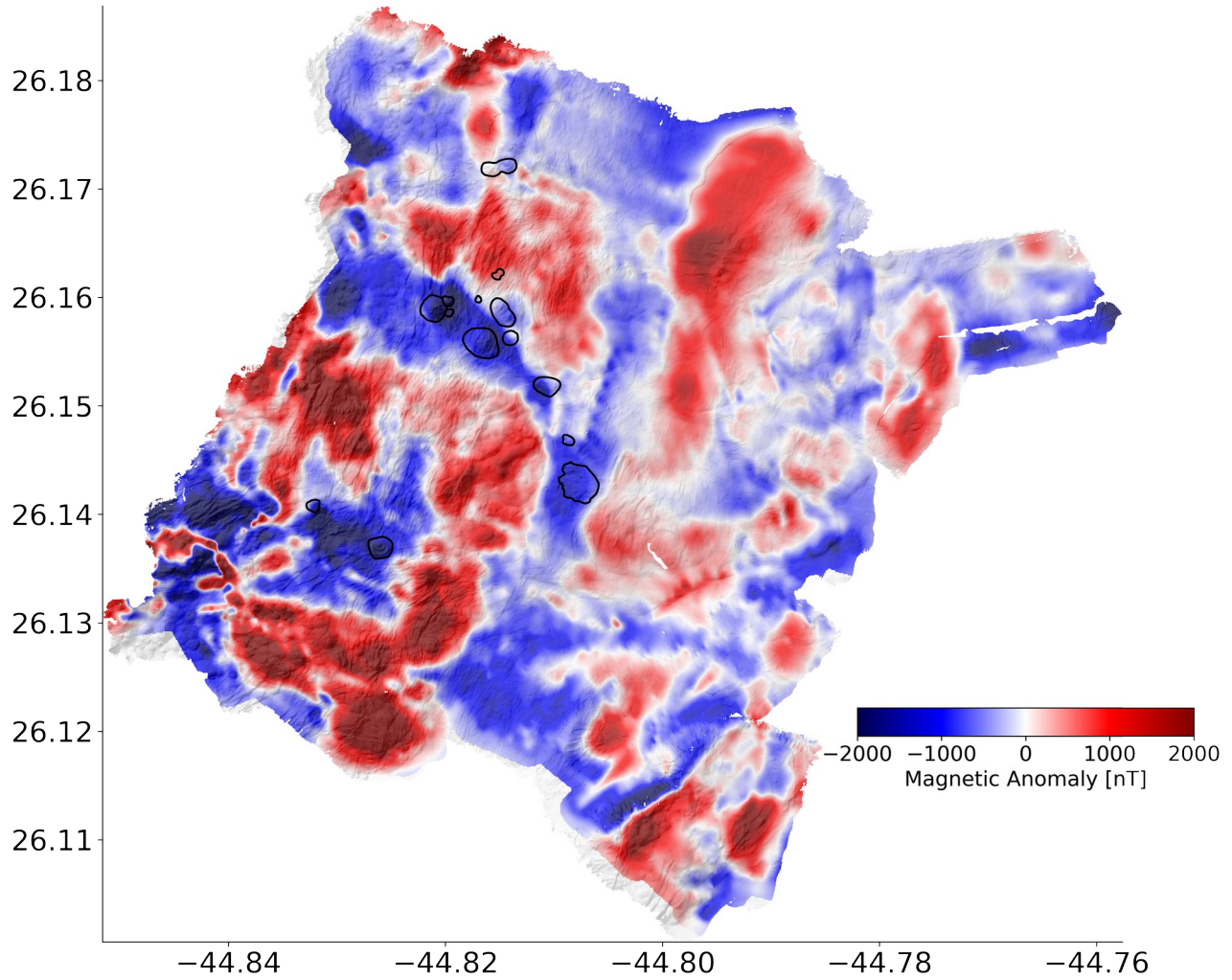


Figure 2: Overlay map of the hillshade bathymetry (2 m resolution) and the magnetic anomaly map with 10 m spatial resolution from Pedersen (2016). Outlined in black are the known SMS mounds depicted by Graber et al. (2020).

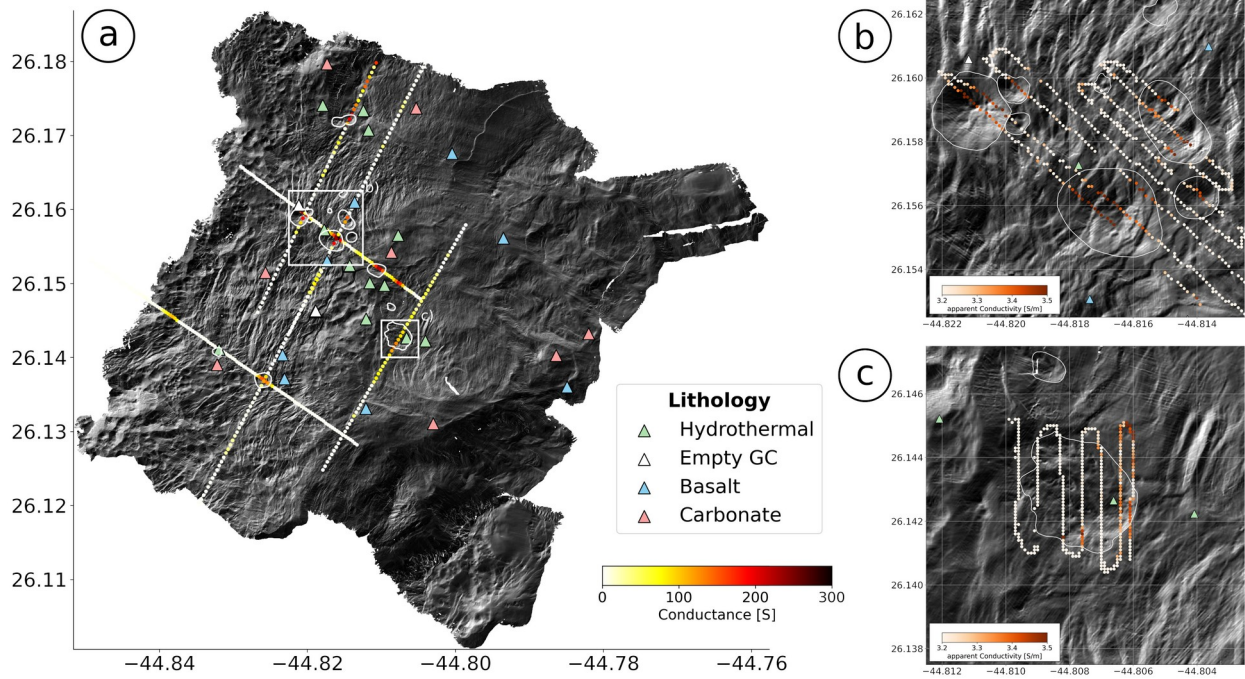


Figure 3: (a) Hillshade map of the bathymetry data with a spatial resolution of 2 m. Computed electrical conductance values derived from 2D CSEM resistivity models of Gehrman et al. 2019 are displayed with color-coded markers. Light colors denote a low and hot colors a high conductance. (b) Zoom-in of the Three-Mound region overlain by the transformed apparent conductivity values obtained by TEM measurements. (c) Same as (b) but for the MIR zone. Outlines of the mounds denote the manually-annotated lateral mound dimensions from Graber et al. (2020). Triangular markers in (a) through (c) illustrate the locations of the 3 m gravity cores and the lithology observed within the core samples (Petersen, 2016).

864
 865
 866
 867
 868

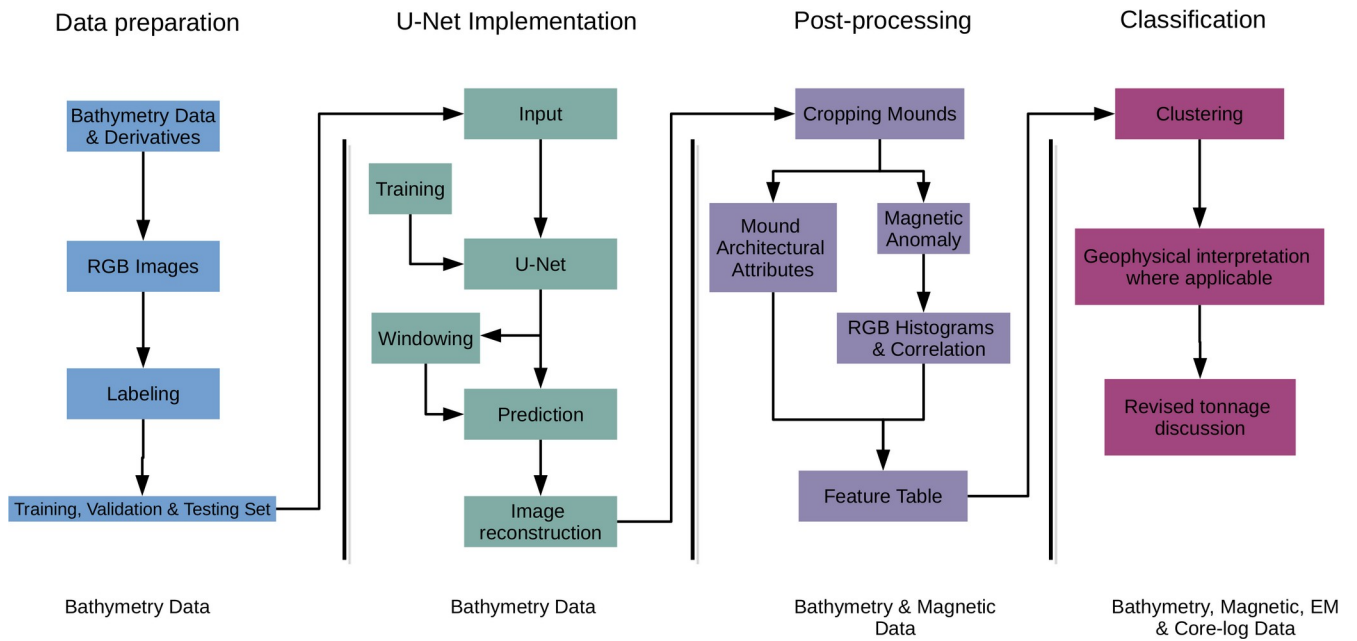


Figure 4: Schematic of the applied workflow including all relevant steps applied, i.e. data preparation, U-Net implementation, post-processing and classification.

870

871 |

872 |

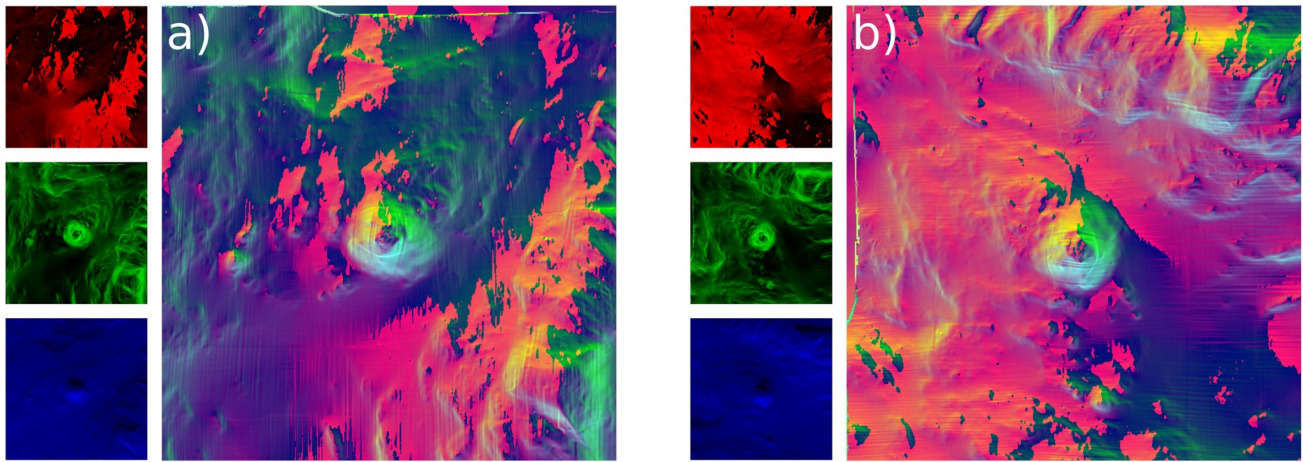


Figure 5: Image unification example of relevant bathymetry features into a common visual representation that is generically applicable to coherently address bathymetry data acquired at different regions across the globe. The aspect, slope, and ∂y derivative of the bathymetry are mapped onto the red, green and blue channels of a standardized 0-255 RGB image (left column of each panel). In this representation, mounds appear directionally invariant with coherent color representation. (a) The original input data and (b) the original input data rotated by 90° . Contrarily, the background bathymetry differs based on the predominant strike direction of the seafloor morphology, whereas prominent mound features remain rotational invariant.

873 |

874 |

875 |

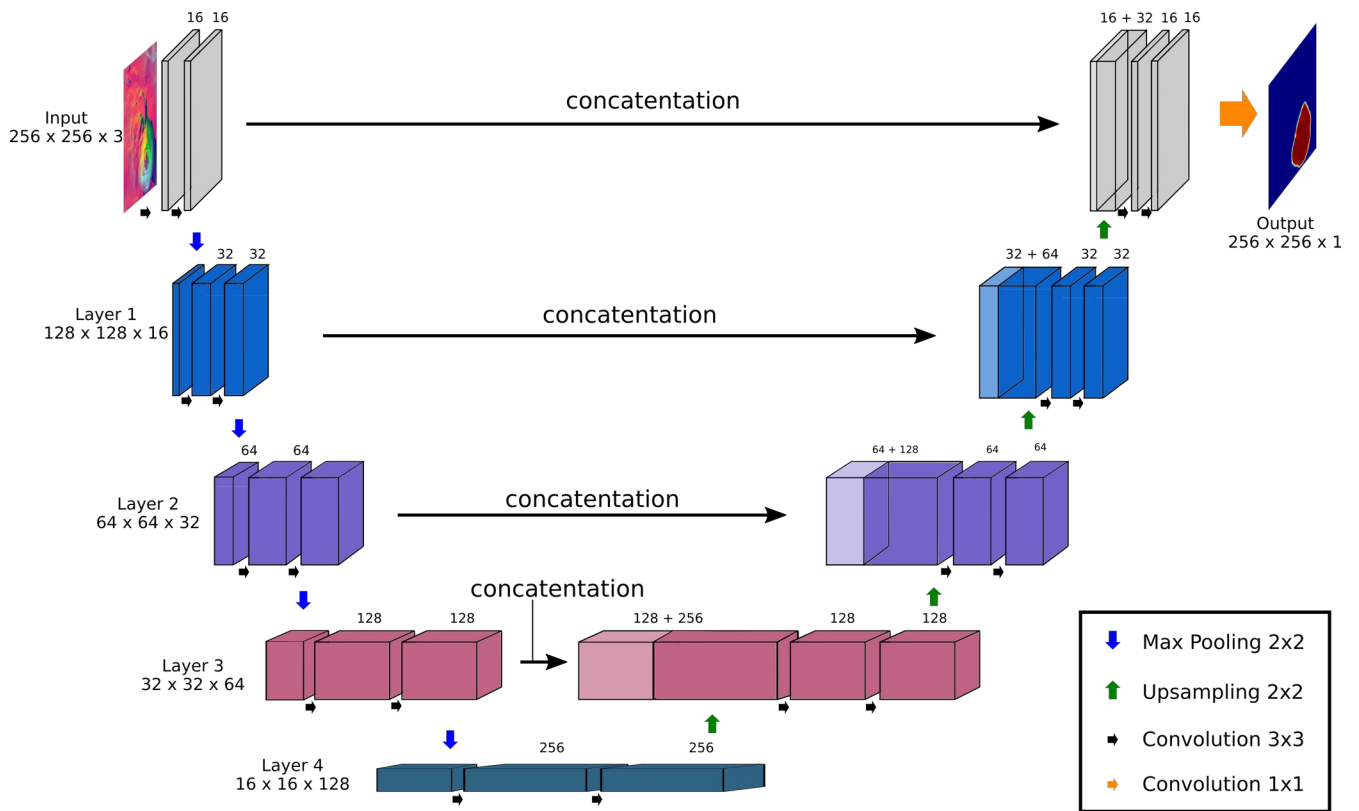


Figure 6: Schematic of the U-Net architecture used for semantic segmentation of the bathymetry data (modified after Ronneberger et al., 2015).

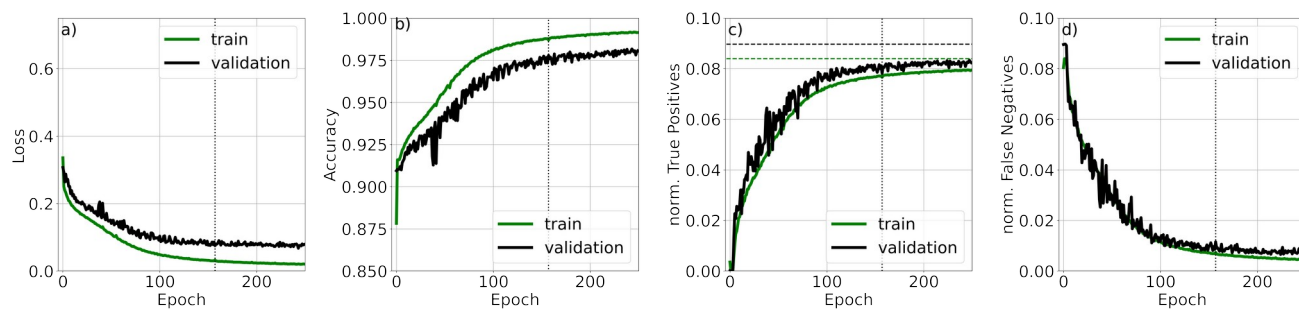


Figure 7: (a) Binary cross-entropy loss function used during training (green) and validation (black). Additional metrics, i.e. (b) accuracy, (c) true positives and (d) false negatives are also used to assess the model performance. Note that true positives and false negatives are normalized to represent percentages of of pixels per image. The vertical dotted line denotes the point of early stopping whereas the horizontally dashed lines in (c) represent the average number of pixels affiliated with mound structure within training and validation data.

880 |

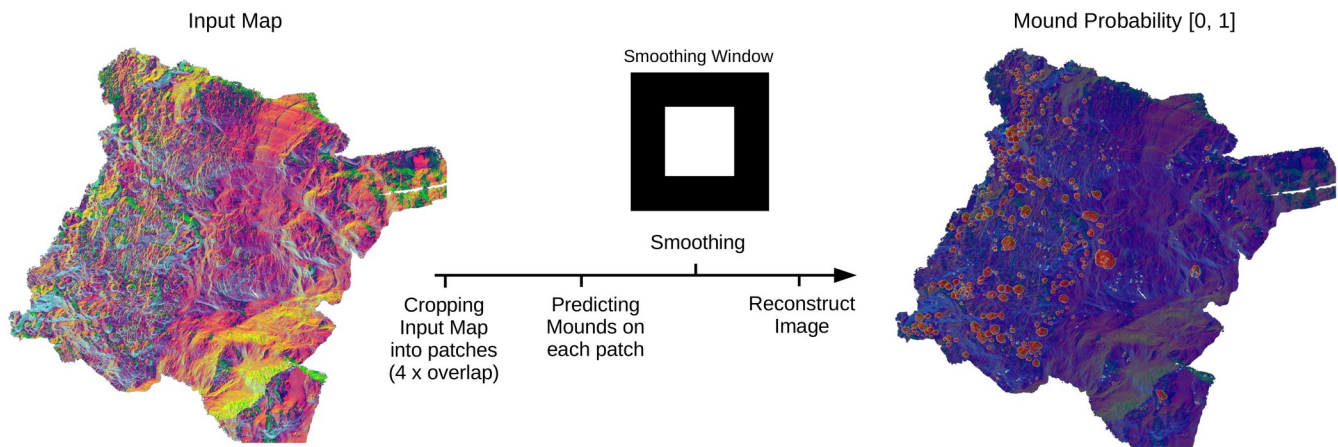
881 |

882 |

883 |

884 |

885 |



Figsiz=(4608, 5120)

Figure 8: Workflow of mound prediction for the AUV bathymetry raster. The pre-processed AUV bathymetry map is cropped into overlapping 256 x 256 patches, which are presented to the U-Net for prediction. The output is smoothed using displayed window where pixels within the black region are neglected due to edge effects that deteriorate predictions (as observed within the testing phase). The right panel shows the final prediction map that is utilized for further processing.

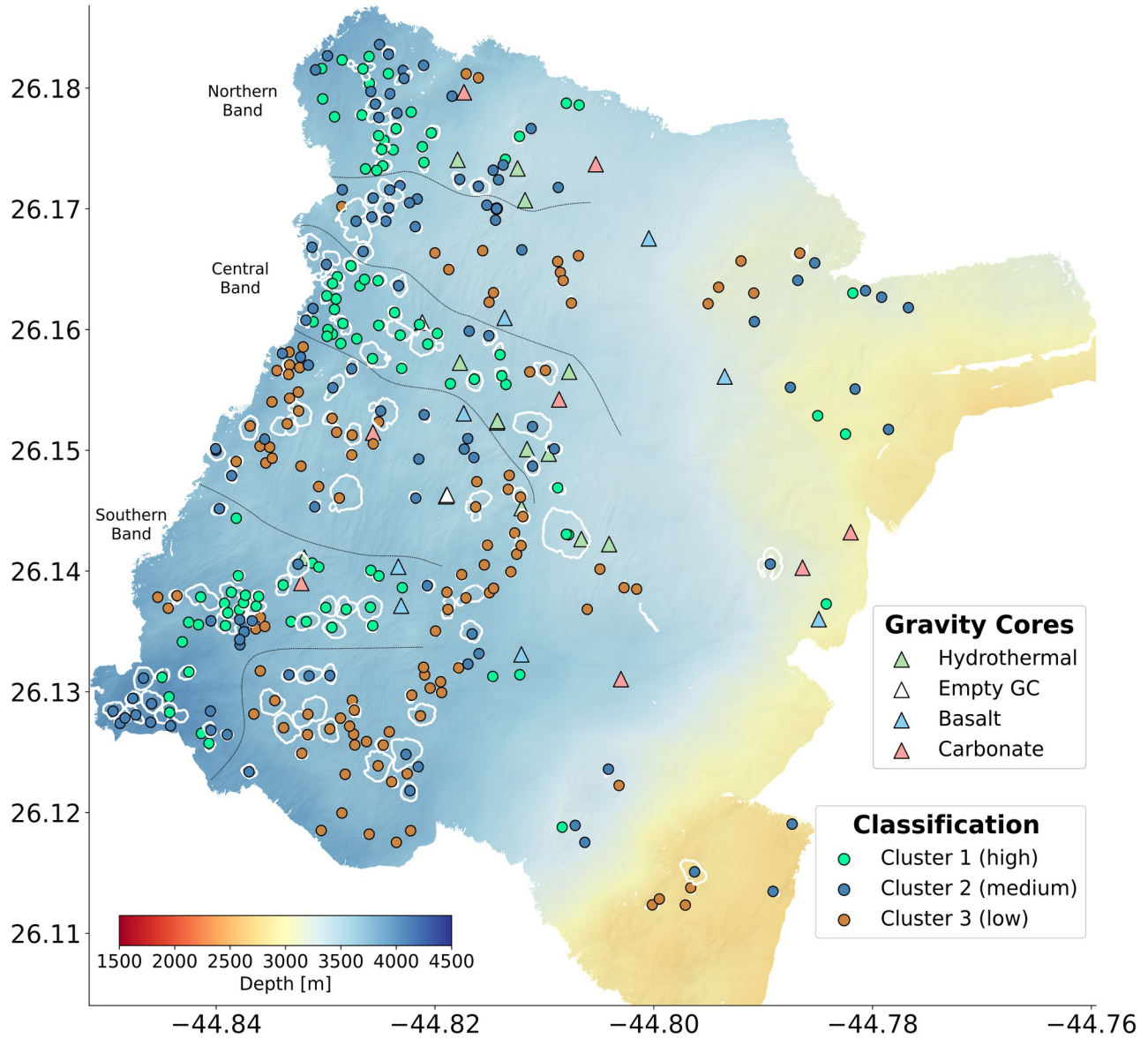


Figure 9: Bathymetry map containing the 323 mounds with a lateral of footprint greater than 290 pixels (1040 m^2) as predicted by the U-Net. The mounds are illustrated by white contours and are classified as either Cluster 1 (high priority), Cluster 2 (medium priority) or Cluster 3 (low priority). Dotted gray lines illustrate the interpreted boundaries of the three latitudinal bands containing hydrothermal edifices.

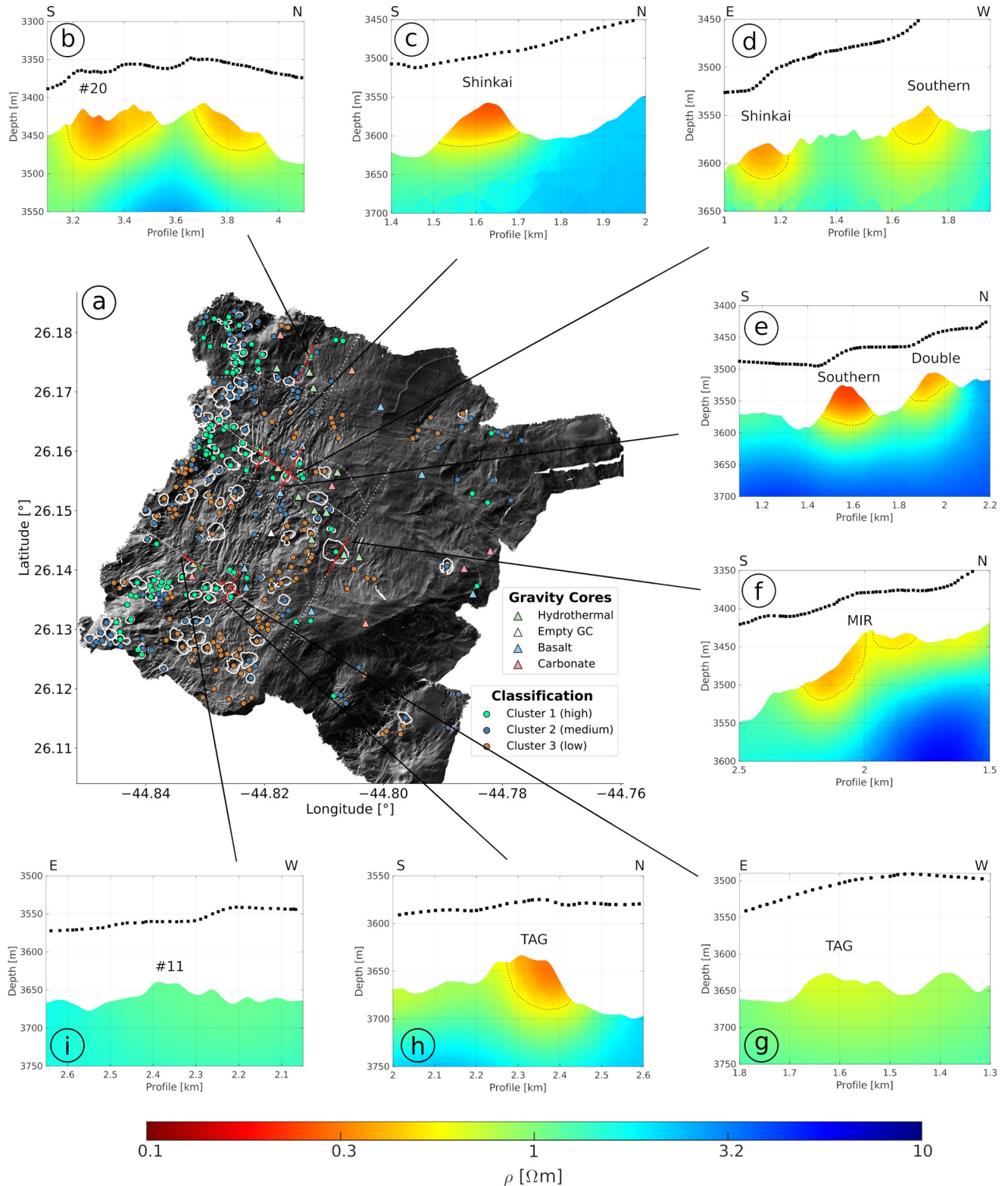


Figure 10: (a) Hillshade bathymetry data with classified mounds as illustrated in Fig. 9. Panels (b) through (i) show electrical resistivity models for each of the high priority mounds intersecting a CSEM profile. The lateral extent of each profile is illustrated by red lines in (a). In (b) through (I), red color shading indicates low resistivity (mineralization), whereas green/blue are more resistive background basalts. Black markers denote transmitter positions along profile.

Automated seafloor massive sulfide detection through integrated image segmentation and geophysical data analysis: Revisiting the TAG hydrothermal field

Amir Haroon^{1,2}, Hendrik Paasche³, Sebastian Graber^{1,4}, Sven Petersen¹, Eric Attias^{5,6}, Marion Jegen¹, Romina Gehrman⁷, Sebastian Hölz¹, Meike Klischies^{1,8}

¹ Helmholtz Centre for Ocean Research, GEOMAR Kiel, Wischhofstr. 1-3, 24148, Kiel Germany

² Hawaii Institute of Geophysics and Planetology, School of Ocean and Earth Science and Technology, University of Hawai'i at Manoa, Honolulu, HI, USA

³ UFZ Helmholtz Centre for Environmental Research, Leipzig, Germany

⁴ Helmut-Schmidt Uni Hamburg

⁵ Institute for Geophysics, Jackson School of Geosciences, The University of Texas at Austin, Austin, TX, USA

⁶ Department of Geology and Geophysics, Woods Hole Oceanographic Institution, Woods Hole, Massachusetts, USA

⁷ Dalhousie University, 6299 South St, Halifax, NS, B3H 4R2, Canada

⁸ North.io GmbH, Einsteinstraße 1, 24118 Kiel, Germany

ORCID IDs

Amir Haroon: 0000-0001-5138-6730; Hendrik Paasche: 0000-0003-1814-0645; Sebastian Graber: 0000-0003-1154-6968; Eric Attias: 0000-0003-4308-1683; Romina Gehrman: 0000-0002-3099-2771; Sebastian Hölz: 0000-0003-2839-9394; Marion Jegen: 0000-0001-6307-8428; Sven Petersen: 0000-0002-5469-105X; Meike Klischies: 0000-0003-4319-4573

Key Points

- Developed two-step machine learning workflow to identify mound structures in bathymetry and classify their origins based on auxiliary data.
- Substantial increase of potential SMS edifices detected within the TAG hydrothermal field distributed within latitudinal bands.
- SMS mineral potential is likely lower than perviously assumed due to heterogeneously distributed mineralization within mounds.

30 **Abstract**

31 Accessible seafloor minerals located near mid-ocean ridges are noticed to mitigate projected metal
32 demands of the net-zero energy transition, promoting growing research interest in quantifying global
33 distributions of seafloor massive sulfides (SMS). Mineral potentials are commonly estimated using
34 geophysical and geological data that lastly rely on additional confirmation studies using sparsely
35 available, locally limited, seafloor imagery, grab samples, and coring data. This raises the challenge of
36 linking in-situ confirmation data to geophysical data acquired at disparate spatial scales to obtain
37 quantitative mineral predictions. Although multivariate datasets for marine mineral research are
38 incessantly acquired, robust, integrative data analysis requires cumbersome workflows and experienced
39 interpreters. Here, we introduce an automated two-step machine learning approach that integrates
40 automated mound detection with geophysical data to merge mineral predictors into distinct classes and
41 reassess marine mineral potentials for distinct regions. The automated workflow employs a U-Net
42 convolutional neural network to identify mound-like structures in bathymetry data and distinguishes
43 different mound classes through classification of mound architectures and magnetic signatures. Finally,
44 controlled source electromagnetic data is utilized to reassess predictions of potential SMS volumes.
45 Our study focuses on the Trans-Atlantic Geotraverse (TAG) area, which is amid the most explored
46 SMS area worldwide and includes 15 known SMS sites. The automated workflow classifies 14 of the
47 15 known mounds as exploration targets of either high- or medium-priority. This reduces the
48 exploration area to less than 7% of the original survey area from 49 km² to 3.1 km².

49

50 **Keywords:** Convolution Neural Networks, Seafloor Massive Sulfides, Bathymetry, Magnetic
51 Anomaly, CSEM

52

53 **Data Availability Statement:**

54 The bathymetry data used for training the U-Net model are available on open-access repositories as
55 listed in Tab. A1. The AUV-bathymetry and magnetic anomaly maps are available from Peterson
56 (2019) (<https://doi.pangaea.de/10.1594/PANGAEA.899415>) and CSEM data from Gehrman (2019) (<https://doi.pangaea.de/10.1594/PANGAEA.899073>).

57

58 1 Introduction

59 Over 700 active, inactive and extinct hydrothermal venting sites (cf. definitions in Jamieson &
60 Gartman, 2020) are known to exist along mid-ocean ridges, volcanic arcs, or back-arc spreading
61 centers (Beaulieu et al. 2015; Beaulieu & Szafranski, 2020). Their existence is documented through
62 hydrothermal plumes that are visually confirmed using a suite of underwater-vehicles (e.g., Murton et
63 al., 2019), towed-camera systems (Beaulieu et al., 2013), or via in-situ probing such as gravity coring
64 (Petersen et al., 2016) or seafloor drilling (e.g., Murton et al. 2019). Understanding the distributions of
65 hydrothermal venting, often associated with the evolution of seafloor massive sulfides (SMS), remains
66 a prevalent research topic motivated by the increased demand of strategic minerals needed to foster the
67 net-zero energy transition. The economic and environmental challenges of modern society interfaces
68 with various fields of marine research to predict where subsurface processes transport mineral-
69 enriched, high-temperature fluids from the deep lithosphere towards the seafloor. In many cases these
70 processes are associated with mineral accumulations that form distinct mound-like expressions (e.g.,
71 Fouquet et al. 2010) often referred to as SMS mounds. Current estimates suggest that the abundance of
72 known SMS can contribute a fractional supply of strategic metals in the future (Hannington et al.,
73 2011), albeit the known uncertainties with respect to size, distribution, volume, as well as the
74 environmental impact that would succeed mining these potential deep-sea resources.

75

76 Tonnage estimates of marine minerals are interpreted from seafloor morphology (e.g. Fouquet et al.
77 2010; Graber et al. 2020), geophysical analyses (Haroon et al. 2018; Gehrman et al. 2019; Murton et
78 al. 2019; Galley et al. 2021), or global extrapolations from deposit occurrences along spreading centers
79 (Hannington et al. 2011). Many studies have focused on previously known SMS sites and their
80 immediate surroundings (e.g. Jamieson et al. 2014; Murton et al. 2019; Graber et al. 2020), likely
81 leading to an underestimation of mapped SMS edifices within a given region. For example, Jamieson et
82 al. (2014) discovered over 400 undocumented SMS edifices through manual analysis of high-resolution
83 bathymetry data along the Endeavour Segment. These findings highlight the prevalent question of
84 *where to sample next and in which spatial resolution?* A question often guided by experience, funding,
85 technological constraints and ship-time availability. Moreover, marine scientists recognize the
86 challenges of differentiating prospective SMS mounds from morphologically comparable volcanic
87 constructions (Jamieson et al. 2014) based on bathymetry data alone. In such cases, multivariate
88 databases that include geophysical, geochemical, and geological data acquired across disparate spatial
89 scales can help to 1) identify regions of interest for more detailed in-situ sampling or visual
90 confirmation studies, 2) optimize the use of ship-time through targeted, pre-informed surveying and 3)

91 improve volumetric estimates of SMS candidates via integrative geophysical analyses. However, to
92 process, analyze and interpret this mass of information, integrative data workflows are pivotal for
93 extracting valuable information optimally, improving decision-making tools for localized sampling, and
94 providing more rigorous estimates of known SMS provinces. Here, machine learning (ML) offers
95 avenues to develop coherent data workflows and processing chains sufficiently generic and thereby
96 transferable across various geological domains and data layers. We demonstrate an ML application
97 together with conventional geophysical analyses to automatically detect mound-like morphology on the
98 seafloor and identify distinct high-interest areas based on auxiliary geological and geophysical
99 information to characterize and quantify mineral-enriched SMS targets.

100

101 Geoscientific studies utilizing ML are progressively increasing in environmental and exploration
102 research (e.g., Bouwer et al. 2022; Koedel et al. 2022). ML applications differ not only in the type and
103 spatial and temporal resolution of the input data, but also in the applied techniques. In marine mineral
104 research, ML applications have applied random forest classification (e.g. Gazis et al., 2018) or neural
105 networks (e.g. Keohane & White, 2022; Juliani & Juliani, 2021), focusing mainly on one or two types
106 of input layers (e.g. seafloor images and/or bathymetry data). However, as interdisciplinary SMS
107 databases grow via contributions from geological, geophysical (e.g. Müller, Schwalenberg,
108 Barckhausen, 2023), biological and geochemical applications, ML workflows are expected to also
109 evolve into more generic implementations to facilitate this growing demand of interdisciplinary marine
110 research.

111

112 Our study leverages existing ML applications previously conducted in the marine environment. We
113 introduce a workflow that integrates concurrent data acquired at different spatial scales to better
114 describe the mineral potential within the Trans-Atlantic Geo-traverse (TAG) hydrothermal field. First, a
115 modified approach adapted from Juliani & Juliani (2021) is utilized to identify mound structures in
116 bathymetry data using a U-Net convolutional neural network. Subsequently, the identified mounds are
117 amalgamated with multivariate geophysical and geological databases to assess potential SMS edifices
118 in greater detail. We test the developed workflow using data described in Petersen et al. (2016) and
119 Murton et al. (2018) during two Blue Mining expeditions (<https://blueminig.eu/>) at the TAG
120 hydrothermal field, and compare the results to manual classification studies of Graber et al. (2020) and
121 Murton et al. (2019). This study extends previously published concepts of marine mineral research,
122 which in most cases use a uni-variate database, by including more diversified, multivariate input layers

123 such as reduced-to-the-pole (RTP) magnetics, controlled source and transient electromagnetics (CSEM
124 and TEM), core and grab samples all acquired across various spatial scales.

125

126 **2 Geological and Geophysical Data**

127 The data used in this study were previously published in scientific literature, i.e. Petersen et al. (2016);
128 Murton et al. (2018); Szitkar et al. (2019); Haroon et al. (2018); Gehrman et al., (2019); Graber et al.
129 (2020); Gehrman et al. (2020); Galley et al. (2021). The following describes relevant aspects of the
130 data, which is needed in the context of the ML implementation. Please refer to the above-mentioned
131 literature for more details on data acquisition and geological/geophysical interpretations. It is important
132 to note that from a data science perspective, the available data introduce *a-priori* bias, as these were
133 acquired with the specific purpose of imaging certain physical parameters that, from a geological
134 perspective, are associated with the evolution of SMS. Thus, unknown correlations that extend beyond
135 the current geological understanding of SMS evolution are likely neglected in the presented ML
136 workflow.

137

138 **2.1 Bathymetry Data**

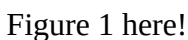
139 Seafloors host numerous focused fluid discharge sites that can appear as mounded manifestations in the
140 seafloor topology (Olakunle et al., 2021). Linking these manifestations to either a volcanic or
141 hydrothermal origin and deriving their potential for forming metalliferous accumulations requires
142 auxiliary data acquired at each specific site. The high-resolution seafloor bathymetry data provides a
143 spatial baseline of where to sample for potential SMS occurrences and also the structural framework
144 for volumetric predictions (e.g., Jamieson et al., 2014; Graber et al., 2020).

145

146 The high-resolution bathymetry data interpreted and classified by the U-Net were collected during
147 research cruise M127 (RV Meteor, 2016) using ship-based multibeam (Fig. 1a) and GEOMAR's
148 Autonomous-Underwater Vehicle (AUV) Abyss (Petersen et al., 2016). Data were acquired using a
149 RESON Seabat 7125 multibeam echosounder, navigated at a speed of three knots using a frequency of
150 200 kHz. The line spacing between adjacent profiles was between 80 m and 100 m at an average
151 altitude of 84 m relative to the seafloor, resulting in a 2 m grid resolution (Fig. 1b). The bathymetry
152 data were processed using the software package MB Systems ([https://www.mbari.org/technology/mb-
153 system/](https://www.mbari.org/technology/mb-system/)) and georeferenced based on prominent seafloor features (Graber et al. (2020) and Szitkar et al.
154 (2019)). This high-resolution bathymetry constructs the baseline of positioning morphological
155 structures during automated segmentation.

156

157 To further optimize the U-Net model, we utilize available high-resolution AUV bathymetry data
158 acquired at different SMS sites around the globe (e.g. Clague et al., 2015; Escartin & Petersen, 2017)
159 and other openly-available bathymetry data. All of the applied bathymetry grids utilized to train,
160 validate and test the U-Net are listed in Tab. A1.

161  Figure 1 here!

162

163 **2.2 AUV-Based Magnetic Data**

164 The magnetic properties of seafloor basalts are dictated by two alteration processes, namely deuteritic
165 oxidation during the initial cooling phase and the superimposed regional hydrothermal alteration that
166 occurs at younger ages (Ade-Hall et al. 1971). During the latter process, high-temperature fluids can
167 cause permanent demagnetization of basalt due to the alteration of titanomagnetite (Szitkar et al. 2020).
168 Thus, RTP magnetic lows constitute an exploration criterion for the recognition of high-intensity
169 hydrothermal discharge zones and potential SMS deposits in the TAG region (Rona, 1978; Rona,
170 1980). They constitute a meaningful geophysical indicator to differentiate between mounds of
171 hydrothermal and volcanic origin within the TAG hydrothermal field.

172

173 During M127, AUV Abyss was augmented by an Applied Physics System (APS) 1540 Digital three-
174 axis miniature Fluxgate-magnetometer recording at 10 Hz. At the time of the cruise, the Earth's
175 inducing field vector had an inclination of 42° , declination of -15° , and field strength of about 38290
176 nT (Galley et al., 2021). Induced and permanent magnetization effects caused by the AUV itself were
177 removed from the magnetic data by conducting figure-eight calibration dives to solve for the AUV's
178 magnetic properties following Honsho et al. (2013). The magnetic data illustrated in Fig. 2a have been
179 interpreted regionally by Sitkar et al. (2019) and locally around the TAG mound by Galley et al.
180 (2021), and are openly available as a 10 m raster (Petersen, 2019).

181

182 AUV drift relative to the bathymetry leads to indeterminate errors that may propagate into the
183 workflow. Using an inertial system, the AUV's lateral position is tracked from the initially calibrated
184 position. However, water column currents may induce gradual shifts away from the inferred position.
185 In comparison to the vertical position of the AUV that is determined through altimeter and depth
186 readings, a lateral shift between the magnetic anomalies and bathymetric features can either be geology
187 driven (cf. Sitkar et al., 2019) or, alternatively, result from positioning errors; both are relevant

188 constraints for the data integration process of the described ML workflow and are addressed in section
189 3.3.

190 Figure 2 here!

191

192 **2.3 Electrical Conductivity**

193 Accumulations of SMS exhibit a distinct contrast in the electrical resistivity compared to the
194 surrounding basalt (Morgan, 2012; Spagnoli et al., 2016). Sulfide mounds are generally more porous
195 compared to the background basalt (Murton et al., 2019), host high-temperature fluids when active, and
196 contain metalliferous minerals and clays, all attributes that contribute to a decrease of the electrical
197 resistivity. Several electromagnetic applications have been proposed to detect and characterize volumes
198 of minerals for example at TAG (Haroon et al., 2018; Gehrmann et al., 2019) or in the Okinawa
199 Trough (Constable et al., 2018; Ishizu et al., 2019; MacGregor et al., 2021).

200

201 **2.3.1 Controlled Source Electromagnetic Measurements**

202 Our controlled source electromagnetic (CSEM) data were acquired using two, fixed-offset Vulcan
203 receivers (Constable et al. 2016) towed at distances of 350 m and 505 m behind a 50-m horizontal
204 electric dipole (HED) source (Sinha et al., 1990). The resulting 2D resistivity models computed with
205 MARE2DEM (Key, 2016) are interpreted and discussed by Haroon et al. (2018) and Gehrmann et al.
206 (2019, 2020). In summary, the CSEM conductivity models highlight distinct regions of known SMS
207 through increased electrical conductivity (cf. Fig. 3a). Here, we use the acquired CSEM data to reassess
208 the electrical resistivity distributions at identified high-priority sites. Electrical conductance illustrated
209 along CSEM profiles qualitatively define spatial extents of conductive, possibly mineral-enriched
210 seafloor, and predict if morphological expressions are associated with hydrothermal (conductive) or
211 volcanogenic (resistive) activity. Notably, Gehrmann et al. (2020) demonstrate that navigational
212 uncertainty of the CSEM system is not trivial in such complex bathymetry, which can result in
213 inversion artifacts. The authors mitigate these artifacts by estimating the data quality on navigational
214 uncertainties such as instrument position with respect to the bathymetry. Here, we further reduce
215 potential inversion artifacts by confining CSEM inversion models to distinct regions associated with
216 mounds, mitigating potential misinterpretations caused by over-fitting the data at irrelevant locations.

217

218 **2.3.2 Transient Electromagnetic Measurements**

219 Marine transient electromagnetic (TEM) data were acquired at two specific sites within the TAG
220 hydrothermal field using GEOMAR's MARTEMIS system (Fig. 3b and 3c). This coincident loop

221 system consists of one transmitter and one receiver loop, which are housed in a $6.3 \times 6.3 \text{ m}^2$ frame. In
222 regions where seafloor conductivity exceeds the water column conductivity, TEM data will exhibit an
223 increased induced voltage allowing a localized inference of SMS distributions. The system is towed at
224 $<1 \text{ kn}$ and 5 – 15 m above the seafloor and records the electromagnetic response of a 50% duty-cycle
225 transmitter signal at 10 kHz. The acquired time series are processed considering the distorting effects
226 described by Reeck et al. (2020) and transformed into full-space apparent conductivity curves
227 following Eq. 1 of Haroon et al. (2018). Regions of increased apparent conductivity are generally
228 associated with areas where the seafloor is more conductive than the water column resistivity ($\rho < 0.3$
229 Ωm), which in our geological setting is indicative of SMS occurrences (Swidinsky et al. 2012).
230 MARTEMIS positioning was computed through an ultra-short baseline (USBL) transponder attached to
231 the tow cable and merged with the processed apparent conductivity data. The spacing between adjacent
232 stations is approximately 10 m (Fig. 3b and 3c).

233 Figure 3 here!

234

235 **2.4 In-situ Data**

236 Overall, 33 gravity cores of max. 3-m length were acquired within the TAG hydrothermal region during
237 the M127 cruise (Petersen et al., 2016). Locations of possible coring sites were selected with the help
238 of the high-resolution AUV bathymetry data. Twenty-three cores contained abundant sediment, eight
239 contained only fragments of gravel, basalt and traces of sediments in the core catcher, and two were
240 empty (Fig. 3, white markers). Among the 23 sediment cores, 10 had visible hydrothermally-influenced
241 indications (Fig. 3, green triangles); the other cores had the visual appearance of background sediments
242 (carbonate ooze) or showed layers of volcanic origin (Fig. 3, red and blue triangles, respectively). Note
243 that the presence of background sediment or empty cores does not rule out hydrothermal activity at
244 greater depth, as penetration of this coring technique was limited to a maximum of three meters.

245

246 In addition to gravity cores, rock drill samples have been drilled to a maximum depth of 12.5 m below
247 seafloor (Murton et al., 2019). The obtained samples from the Southern, Rona and MIR mounds show
248 high concentrations of minerals, confirming the hydrothermal origin of these three mounds. Here, we
249 link core sites indicative of hydrothermal alteration with collocated EM resistivity data and models to
250 distinguish spatial extents of mineral zones on these mounds and reassess tonnage estimates.

251

252

253

254 **3 Methods**

255 The workflow is split into four steps as illustrated in Fig. 4: 1) selecting and preparing suitable mid-
256 ocean ridge (MOR) bathymetry data, e.g. from accessible open-source data repositories (Tab. A1), 2)
257 training, validating and testing the U-Net model, 3) post-processing of the model output to derive
258 mound architectures and integrate with concurrent RTP magnetic data, and 4) classification and
259 geophysical analysis of identified mounds. The workflow is scripted in Python (Ver. 3.8.12) and uses
260 the Tensorflow (Ver. 2.4.1) library for machine learning tools.

261 

262

263 **3.1. Data Preparation: Bathymetry Data**

264 Bathymetry data used for training are identified as suitable, if a large spatial coverage is acquired at
265 either MORs or at specific hydrothermal fields. Bathymetry rasters are subdivided into overlapping
266 patches of 256 x 256 pixels with a step length of 128 pixels. These pixels are manually annotated using
267 a binary representation, where pixels associated with mounds are labeled as *True* and all other pixels
268 are labeled as *False*. In total, 1899 mounds were manually annotated using the bathymetry data listed in
269 Tab. A1.

270

271 To appear in a common standard that highlights rounded convex and concave morphology through
272 distinct representations, we use a multi-directional slope analysis by mapping the normalized aspect,
273 slope, and the ∂y derivative onto Red, Green and Blue channels of a standardized RGB image,
274 respectively (Fig. 5). The chosen approach converting certain derivatives of bathymetry data into single
275 RGB images facilitates a generalized visual interpretation and aids the model performance. All
276 resulting images show the north flank of mounds in yellow to green moving west to east. Southern
277 mound flanks appear white to blue. Concave features such as pits appear in a reversed manner.

278

279 Note that directional dependencies of background features in the preprocessed images remain unaltered
280 through pre-processing (Figure 5). To increase the amount of training data and mitigate learning of
281 directional dependencies in various settings, input bathymetry was augmented by means of a 90°
282 rotation. As mound structures are near-circular structures, they remain rotational invariant although
283 background strike differs (cf. Fig. 5a and b). In total, 2280 RGB images were produced to train,
284 validate and test the U-Net model, each consisting of 65,536 pixels.

285 

286

287 **3.2 U-Net Implementation, Training and Evaluation**

288 The model architecture yields an end-to-end trainable neural network including segmentation of input
289 images into partitioned pixel sets of corresponding classes. This type of network was first introduced
290 for biomedical image segmentation by Ronneberger et al. (2015) and resembles a symmetric “U” (Fig.
291 6). In our specific case, the U-Net model distinguishes mound from background features and provides
292 values of probabilities (Hu et al., 2015) as outputs.

293

294 For training and testing, only images with at least two percent of the pixels annotated as mounds were
295 considered. Of these, 75 percent were used for training, 20 percent for validation and 5 percent for
296 testing. We use the binary cross entropy loss function defined as:

$$297 \quad H_p(q) = \frac{1}{N} \sum_{i=1}^N y_i \cdot \log(p(y_i)) + (1 - y_i) \log(1 - p(y_i)) \quad (1)$$

298 where y_i refers to the corresponding binary label of each pixel and $p(y_i)$ to the predicted value between
299 0 and 1 within each Epoch i of training. The accuracy, true positive and false negative metrics were
300 computed to determine a point of early stopping, i.e. a model with sufficient accuracy and minimal
301 over-fitting (Fig. 7). The model outputs are contoured at values of >0.5 to outline lateral mound
302 dimensions of the mound pedestal.

303

304 After training, the pre-processed AUV bathymetry image from the TAG area (Petersen, 2016) is
305 presented to the U-Net model as overlapping patches of 256 x 256 pixels. The image reconstruction
306 process is illustrated in Fig. 8. To prevent inaccurate predictions along the image edges, an image
307 smoothing considers only the central 128 x 128 pixels. The outer edges of each predicted patch are
308 neglected. Using an overlapping process, each pixel of the bathymetry grid is included four times
309 within the output prediction. The maximum probability from the four predictions is used as the final
310 pixel probability.

311

312 **3.3. Post-processing of mound structures**

313 The output mound contours define the location and lateral footprints of each mound, which is
314 calculated (in m^2). A minimum threshold of $\sim 1040 m^2$ mound footprint (290 pixels) is introduced to
315 remove most of the falsely detected mound structures caused by geological noise and to focus the
316 analysis on potentially significant SMS volumes (cf. Murton et al. (2019) for discussion). From each of
317 the mound contours, we compute the lateral footprint, maximum height, and median slope using only

318 pixels located within each mound contour. These parameters are used to describe the general mound
319 architecture and are used as inputs for classification.

320

321 For integrating the magnetic anomaly data with the detected mounds from the UNet, an image overlay
322 of gray-scaled hill shade and a diverging red-to-blue magnetic anomaly map (Fig. 2) is cropped and
323 centered around each mound contour, including also peripheral areas. Using the specific red-blue color
324 representation, RTP anomalies appear either red (if positive) or blue (if negative), both being primary
325 color channels within an RGB color spectrum. Color histograms and correlations of the three RGB
326 channels depict positive, negative or a mixture of RTP anomalies into three single values, depending on
327 whether the image is blue, red, or a blue/red blend. The channel correlations serve as inputs for the
328 subsequent classification of the mounds.

329

330 **3.4. Classification & Evaluation**

331 We applied spectral clustering using the Sci-Kit Learn Python Library on the derived parameters for
332 each mound contour. Where available, we added peripheral SMS indicators derived from gravity cores,
333 electromagnetic data and known SMS edifices to determine mound evolution and assess the mineral
334 potential at confirmed high-priority sites. This ensemble of derived morphological expressions and
335 geological/geophysical characteristics was integrated into a new model for the formation of SMS
336 mounds in the TAG hydrothermal field. Further, it provides the basis to re-discuss the resource
337 potential of the field.

338

339 **4 Results**

340 *U-Net analysis*

341 The U-Net metrics indicate an optimal point of early stopping at around Epoch 158 (Fig. 7) . There, the
342 network reached a prediction accuracy of greater than 98.6 and 97.8 percent in training and validation,
343 respectively. The training loss reached 0.032 and the validation loss 0.075 (green and black curves,
344 respectively, in Fig. 7a) using a learning rate of 10^{-4} . A learning trend is observable in the ensuing
345 epochs especially within the training data. Yet, the trend is less pronounced within the validation data,
346 indicating that predictions will not improve for unseen images. To analyze the efficiency of the model,
347 accuracy, true positives and false negatives are also utilized to understand the general characteristics of
348 U-Net predictions (Fig. 7 b-d and Tab. 1).

349

350 Manually annotated mound structures make up, on average, less than 8.2 and 9.1 percent of the total
 351 pixels in each of the training and validation images, respectively. This significant imbalance compared
 352 to background leads to a high starting accuracy of approximately 91 percent, assuming that all pixels
 353 are predicted as background, i.e. *False*. Other metrics, such as true positives and false negatives are
 354 more significant for such imbalanced problems. At the point of early stopping, the trained network can
 355 retrieve 87 percent of the true positive pixels in the validation data, meaning that manually classified
 356 mound pixels are also classified as mound affiliated pixels by the U-Net. Similarly, false negatives are
 357 minimized to less than 1 percent of the total pixels per image during training and validation, indicating
 358 only few background formations are being falsely classified as mounds.

359
 360 In addition to these training metrics, 114 images were used as a test dataset to further assess the U-
 361 Net’s efficiency and prediction characteristics for unseen data. A summary of the test data metrics is
 362 listed in Tab. 1. A prediction accuracy of >97.6 percent is achieved for the test data. Model efficiency
 363 in predicting true positives and avoiding false negatives is comparable to the validation data. Note that
 364 there is some bias to consider in the evaluation of these pixel-based metrics. Discrepancies in mound
 365 dimensions between manual annotation and automated segmentation will reduce model performance,
 366 although a mound is essentially detected by the network. In the majority of studied cases within the test
 367 data, mounds were detected and metric deficiencies arise from discrepancies in lateral mound
 368 extensions between manual and automated annotation (see Fig. S1 of supplementary materials).

Table 1: Metrics and corresponding benchmarks of the applied U-Net model for training, validation and testing images.

Metric	Training		Validation		Test	
Accuracy	<i>Benchmark: 0.91603</i> <i>Prediction: 0.98696</i>		<i>Benchmark: 0.9103</i> <i>Prediction: 0.97790</i>		<i>Benchmark: 0.89777</i> <i>Prediction: 0.976976</i>	
True Positives	<i>Benchmark: 0.08397</i> <i>Prediction: 0.07659</i>	91.2%	<i>Benchmark: 0.08970</i> <i>Prediction: 0.07816</i>	87.1%	<i>Benchmark: 0.10223</i> <i>Prediction: 0.088996</i>	87.1%
False Negatives	<i>Prediction: 0.00738</i>		<i>Prediction: 0.01154</i>		<i>Prediction: 0.01323</i>	

369
 370 The trained U-Net detects a total of 323 mounds within the mapped 49 km² of the AUV bathymetry
 371 data (Fig. 9), each with a lateral footprint greater than 1040 m² (= 290 pixel). The predictions include
 372 all previously identified SMS mounds (cf. Fig.1 and Fig. 9). The lateral mound dimensions match, in
 373 most cases, the manual annotation. However, the U-Net model underestimates the spatial footprint for
 374 Southern and Double Mound. Both mounds show a tectonized surface texture, deviating from an
 375 idealized mound shape, which may explain the reduced model performance. The total number of

376 known mounds accumulates to 16 (compared to 15 of Gehrman et al. 2019) because Double Mound is
 377 segmented as two individual peaks by the U-Net classification.

378

379 The output mounds can be classified into three distinct clusters (Fig. 9) using the elbow method applied
 380 during spectral clustering (K-means). Table 2 lists some statistics for each cluster, including the
 381 minimum, maximum, and mean mound dimensions. The number of associated known SMS sites
 382 defines the priority of each cluster to host SMS. Cluster 1 is assigned a ‘high’ priority, as 10 out of 98
 383 mounds are known to host SMS. A ‘low’ SMS priority is assigned to cluster 3 (1 known SMS site out
 384 of 114 mounds), and ‘medium’ to cluster 2 (4 known SMS sites out of 111 mounds).

Table 2: Clustering statistics of output mounds, including the total area of all mounds and associated mound dimensions. The number of known SMS sites associated with each cluster defines the SMS priority of the cluster.

Cluster # (SMS priority)	Number of Mounds	Number of known SMS sites per Cluster	Total Area of all Mounds	Footprint	Height
1 (high)	98	10	982314 m ²	Max: 141310 m ² Min: 1052 m ² Mean: 10024 m ²	Max: 58.62 m Min: 1.35 m Mean: 14.46 m
2 (medium)	111	4	1188213 m ²	Max: 78268 m ² Min: 1205 m ² Mean: 10704 m ²	Max: 52.53 m Min: 0.35 m Mean: 14.98 m
3 (low)	114	1	942423 m ²	Max: 75269 m ² Min: 1094 m ² Mean: 8266 m ²	Max: 56.34 m Min: 1.12 m Mean: 13.62 m
Total	323	15	3112950 m ²		

385

386 The clustering is primarily driven by the magnetic anomaly data (cf. Fig. S2 and S3); therefore, 10 of
 387 the 15 known SMS sites fall in Cluster 1, showing a distinct negative magnetic anomaly. At these 10
 388 mounds, Sztikar et al. (2019) interprets the magnetic anomalies to represent a vertical hydrothermal
 389 conduit centered above their corresponding source. Known SMS sites of Cluster 2 (4) show both
 390 positive and negative RTP magnetic anomalies indicating either geological alteration or poor AUV
 391 navigation. Cluster 3 contains only one previously known SMS site (Mound #24 from Graber et al.
 392 2020) that is associated with a positive magnetic anomaly. Images of all clustered mounds are
 393 displayed in Fig. S2 of the supplementary materials.

394

395 Despite their magnetic signature, mound morphology is similar in all clusters with respect to their mean
396 heights and mound footprints (cf. Tab. 2 and Fig. S3 in the supplementary materials). Other
397 morphological features indicative of hydrothermal activity, such as jagged contours and number of
398 peaks (Jamieson et al. 2014), could not be identified by our workflow as important parameters for
399 differentiating mound evolution in the TAG area. This leaves the magnetic anomaly as the strongest
400 spatial indicator in the available data set.

401

402 *Spatial Distribution of Morphological Features and Magnetic Footprint*

403

404 The high-priority sites (Cluster 1) occur spatially confined in three bands (labeled Southern, Central
405 and Northern Band in Fig. 9). All bands strike NW-SE, roughly perpendicular to the axis of the Mid-
406 Atlantic Ridge, and coincide well with interfaces between different structural domains identified by
407 Graber et al. (2020). The southern band lies within a region of oblique faults and fissures (Fig. 8 of
408 Graber et al. 2020), that have been suggested to promote upward migration of hot fluids at TAG and
409 other regions (Anderson et al. 2015). The central band of mounds is located within the NW-SE
410 extension of the, so-called, Three-mound area (cf. Graber et al., 2020), runs parallel to mapped
411 corrugations, and connects the Three-Mound regions to the MIR zone (Fig. 9). The northern band lies
412 north of a zone with chaotic seafloor morphology and positive magnetic signature, separating the
413 smooth bathymetry and negative anomalies of the central and northern bands.

414

415 The alignment of Cluster 1 mounds is interrupted in several locations. In the southern band, at around
416 26.138°N and 44.837°W, Cluster 1 mounds are not associated with oblique fissures mapped by (Graber
417 et al. 2020). Instead, negative magnetic anomalies correlate with ‘fresh’ pillow mounds. Such
418 potentially younger magmatic features may mask the oblique fissures typical for the southern band.
419 The northern band contains only one known hydrothermal site named Shimmering, but multiple gravity
420 cores indicate an abundance of hydrothermally-altered sediments in the area (cf. Fig. 9). However,
421 mounds located at the western section of the northern band are structurally interpreted as pillow
422 mounds (Graber et al. 2020).

423

424 *Analysis using Electromagnetic Data*

425 SMS potentials have often assumed homogeneously distributed metal grades across a mounds
426 morphological footprint and its corresponding stockwork zone. Although tonnage estimates are often
427 based on in-situ measurements (i.e. core-log data/seafloor drilling), derived mineral potentials are

428 likely too optimistic because in-situ data are 1) available at only few representative mounds, 2)
429 generally obtained at the points of highest interest, i.e. where SMS is apparent in seafloor imagery and
430 3) penetrate only few meters into the subsurface. In the majority of cases, the structural heterogeneity
431 of individual mounds is either neglected or considered too simplistic, assuming that SMS with high
432 metal grades are distributed across the entire lateral extent of each mound. To constrain this rather
433 generalized assumption, resistivity models derived from CSEM or TEM data appear more suitable to
434 understand the degree of mineralization away from the point-scale core-log data.

435

436 Here, we focus on the electromagnetic data acquired only along high-priority mounds (Cluster 1) or
437 verified mounds that have been documented in preceding literature. CSEM resistivity models that were
438 recomputed for Cluster 1 mounds are illustrated in Fig. 10 using data acquired by Gerhmann et al.
439 (2019). Note that only those mounds are considered that are intersected by CSEM transects. Regions of
440 low resistivity are illustrated by red to orange coloring, background resistivity through green and blue
441 coloring.

442

443 The CSEM resistivity models illustrate that the majority of investigated Cluster 1 mounds are
444 associated with a distinct low-resistivity anomaly of variable magnitude. This, together with core-log
445 data and grab samples (Peterson et al. (2016); Murton et al. (2019)) confirms a certain degree of
446 mineralization at each of the prospective sites. It needs to be noted that in a few instances, i.e. Fig. 10d
447 and 10g, CSEM data has only limited resolution due to the large vertical offset between measurement
448 system (denoted by black markers) and seafloor, thus, limiting a quantitative analysis of mineral grades
449 using CSEM data. Laterally, resistivity distributions and amplitudes do indicate a high degree of
450 certainty and illustrate characteristics of mound composition. Shinkai and Southern mounds, residing in
451 the central band (Fig. 10c through 10e) exhibit a relatively homogeneous conductive structure. These
452 two mounds appear as low-resistive anomalies across their entire lateral footprint (cf. apparent
453 conductivity data in Fig. 3b) indicating that previous mineral estimates could be accurate. In contrast,
454 Double (Fig. 10e) and Rona (Fig. 3b) mound exhibit a low resistive anomaly only in the vicinity of
455 their peaks with no notable contrast to the background resistivity at their pedestal. Although, Rockdrill
456 cores of up to 12 m acquired at the peak of Rona confirm high metal concentrations within a sulfide
457 layer (Murton et al., 2019), TEM data indicates that the majority of Rona's volume is of lower
458 economic value due to a missing apparent conductivity anomaly (Fig. 3b).

459

460 MIR mound has the largest spatial footprint of Cluster 1 mounds in the study area (Fig. 10f). Previous
461 predictions based on mound volumes and extrapolated metal grades derived from gravity cores and
462 rock drill data suggest MIR to be the most economical site within the TAG hydrothermal field (Graber
463 et al. 2020). CSEM inversion of MIR illustrated in Fig. 10f shows an irregular distribution of low-
464 resistive zones across the mound transect indicating the presence of mineralized sediments, but not in
465 the quantity suggested by previous studies. The higher resolution TEM data acquired along multiple
466 transects across the MIR mound support this hypothesis (Fig. 3c) contradicting the notion of MIRs high
467 mineral potential. The point-scale gravity core and Rockdrill data (Peterson et al. (2016); Murton et al.
468 (2019)) were acquired in the northwestern region of the MIR contour, where high apparent
469 conductivities exist. Most of the other regions of the mound structure are not associated with a distinct
470 resistivity anomaly, thus, indicating that mineralization is irregularly distributed across MIR and that
471 tonnage predictions for MIR may be significantly overestimated.

472

473 TAG is arguably the most prominent mound in the study area. Multiple geophysical and geological
474 surveys have focused on the internal mound structure, including the Ocean Drilling Program (ODP)
475 Leg 158 experiment (e.g. Humphris et al., 1995). As such, the internal structure of TAG is well
476 constrained and serves as a blueprint for estimating mineral potentials for other mounds, where less
477 knowledge about internal structure and data are available. The CSEM resistivity models of TAG (Fig.
478 10g and 10h) show an E-W and N-S transect crossing the mound, respectively. Unfortunately,
479 navigation during the E-W transect was chosen too conservative with towing altitudes exceeding 100 m
480 above seafloor, which resulted in inadequate resolution for the TAG's resistivity structure. However,
481 the N-S profile (Fig. 10h) is intriguing, as it supports the asymmetric distribution of mineralization
482 presented in previous studies (e.g Galley et al. 2020). Moreover, the CSEM resistivity model indicates
483 that a significant resistivity contrast compared to the background basalt may only exist for the massive
484 pyrite, pyrite-anhydrite, pyrite-silica and possibly the pyrite silica units (see Knott et al. 1998). Hence,
485 the applied CSEM configuration is likely unsuitable for detecting the stockwork structure and requires
486 higher resolution CSEM data acquired in a 3D survey as demonstrated by MacGregor et al. (2021).

487

488 5 Discussion

489 5.1 Automated SMS Mapping using Machine Learning

490 The presented workflow can be used as a blueprint for prioritizing SMS exploration targets at mid-
491 ocean ridges and understanding distributions of mineral potentials. The workflow reduces the total area
492 of interest from the surveyed 49 km² to 3.1 km², which in turn can be further reduced to either 1.92 km²

493 (Clusters 1 and 2) or 0.98 km² (only Cluster 1) using additional magnetic constraints (i.e. mounds with
494 magnetic lows). Moreover, the latitudinal bands of hydrothermal activity identified through this
495 integrated analysis reveal prospective areas where to search for SMS and may also exist at other
496 MORs. The workflow is fully automated, allowing us to identify regions of interest in quasi real-time
497 (if a pre-trained model exists) when new data is acquired, thus, reducing exploration costs considerably
498 and permitting more focused surveying. Additionally, the workflow is adaptable to future developments
499 in marine mineral exploration and research and its application in other survey areas with similar or
500 additional data layers appears feasible.

501

502 The data preparation part of our workflow seeks to unify the bathymetry data, acquired at different
503 spatial resolution and at various sites across the globe, into a common representation independent of the
504 actual depth, slope, and curvature within a given area. Juliani & Juliani (2021) propose a principal
505 component analysis (PCA) consisting of both a change in slope and a multi-directional shading of
506 elevation data in order to reduce the bathymetric inputs. However, our analysis shows that PCA may
507 not generalize well for bathymetry data acquired at different regions with variable roughness and
508 geological strike. A key advantage of our proposed processing scheme is notably that bathymetry data
509 from different regions will unify onto a single coherent visualization.

510

511 Moreover, the workflow also allows to test and use other types of ML segmentation tools, and to
512 include additional data layers (e.g. high-resolution backscatter, self-potential, etc). As many of these
513 additional data layers are currently not available in open-access repositories, they can be integrated
514 best within the post-processing step. As backscatter and self-potential data become more readily
515 available, it is also feasible to train the U-Net directly for different types of mound characteristics. The
516 integration of such additional data will likely increase ambiguity, but presumably achieve higher
517 certainty in identifying SMS sites.

518

519 Following Szitkar et al. (2019) and Rona (1978; 1980), hydrothermal mounds within the TAG
520 hydrothermal field are associated with a distinct negative RTP magnetic anomaly, whereas volcanic
521 edifices typically display positive values. This characteristic proves suitable for clustering depicted
522 mound contours into groups to identify their potential origins. However, three aspects must be
523 considered to integrate the magnetic footprint of a mound or a group of adjacent mounds with the
524 corresponding bathymetry attributes.

525

- 526 1. Magnetic anomaly data are acquired at a resolution of 10 m grid spacing compared to the 2 m
527 resolution of the bathymetry data. A pixel-wise comparison between magnetic anomalies and
528 morphological features requires an up-sampling of the magnetic anomaly data, which may lead
529 to interpolation artifacts.
- 530 2. An RTP magnetic anomaly shows magnetization and geomagnetic field vectors that render
531 vertical anomalies above the causative body. However, Szitkar et al. (2019) discuss that tectonic
532 events can tilt the crustal block causing altered shapes of the magnetic anomalies, leading to
533 incoherent magnetic anomalies associated with morphological expression. A similar effect is
534 also observable if tectonic forces act on a previously deposited mound.
- 535 3. AUV magnetic data are susceptible to errors that arise from inaccuracies in AUV positioning
536 relative to its calibrated coordinates. This may lead to a lateral shift between the morphological
537 expression and the corresponding RTP magnetic anomaly.

538

539 All three undetermined circumstances lead to uncertainties in a pixel-wise integration of the magnetic
540 and corresponding bathymetry pixels. Hence, a relaxation of spatial similarities between mound
541 structures and resulting magnetic anomalies is required and was implemented in our analysis.

542

543 The approach would benefit from a greater number of annotated bathymetry data available in online
544 repositories to improve model training. The chosen study area belongs to the most studied
545 hydrothermal sites globally, and, provides a solid first training set. The developed workflow focuses on
546 the analysis of high-resolution bathymetry data, which resemble the most common collected data in
547 seafloor exploration. Given the steady increase of sea-going SMS research, manual assessments of each
548 individual data layer becomes increasingly difficult and automatization of workflows will be inevitable.
549 Therefore, application of the workflow in other hydrothermal areas either at mid-ocean ridges or other
550 geological environments with complex, rough terrain, is a crucial future task.

551

552 ***5.2 Implications for hydrothermal activity in the TAG area***

553 Notably, marine mineral exploration is a complex endeavor unlikely solved by a silver bullet approach.
554 Thus, various ML strategies and conventional geoscientific research will attest a feasibility for
555 detecting SMS and estimating mineral potentials. The proposed ML strategy does not contradict this
556 notion, but instead, offers a means of integrating multivariate data into a common interpretation scheme
557 that is easily audited. Note that the delineation of convex structures in bathymetry data underlies some
558 variability resulting from terrain analysis and, even if conducted manually, remains ambiguous due to

559 interfering geomorphic processes that mask or distort typical mound morphologies. Hence, although
560 mapping the correct mound dimensions is significant for addressing mineral potentials, discrepancies
561 between manual and automated segmentation are expected.

562

563 Despite these explainable deviations, the spatial alignment of Cluster 1 bands is clearly visible and the
564 correlation to structural domains defined by Graber et al. (2020) is apparent. This may support the
565 hypotheses of a structural heterogeneity within the hydrothermal field dictating the distribution of SMS
566 edifices, as proposed by Graber et al. (2020). Both the spatial extent of the alignment and the
567 occurrence of deviating areas indicate a structural constraint in the deep subsurface. This dominant
568 structural constraint supports an interpretation where a strongly distorted subsurface structuring (e.g.
569 bend detachment fault) leads to focused fluid flow in the deep subsurface that results in linear, off-axis,
570 distribution of hydrothermal edifices. Moreover, the various upflow zones are likely to span a region
571 larger than the investigated area of study. Further sites may be located north of Shimmering and also
572 south of TAG, as well as in the westward extension of the three bands. Conclusively, the presented
573 workflow has demonstrated a successful amalgamation of spatially acquired bathymetry and magnetic
574 data, which could be used to inform future AUV bathymetry and magnetic surveying.

575

576 Although the number of potential SMS sites drastically increased through this automated analysis,
577 mineral potential of the TAG hydrothermal field is likely lower than originally presumed.
578 Electromagnetic data illustrates that mineralized zones for the largest proposed SMS sites are generally
579 heterogeneously distributed across the mound contour, thus, contradicting the proposed high tonnage
580 estimates using homogeneously distributed mineral grades derived from point-scale measurements. We
581 propose that future analysis of SMS tonnages should incorporate multiple seafloor drillings conducted
582 across the mound contours with additional data layers (e.g. backscatter, seismics, and 3D CSEM
583 inversion models) to achieve a high degree of certainty in the tonnage estimation. If such high-
584 resolution survey strategy for SMS sites is economical, remains beyond the scope of this study.

585

586 The current SMS priority depends mainly on AUV magnetic data and on the number of known SMS
587 sites within a given cluster. The former is not typically considered a conventional data layer in SMS
588 exploration and should be added to the necessary SMS exploration criteria. Furthermore, it cannot be
589 ruled out that future endeavors may potentially change the presented prioritization of SMS mounds
590 through more SMS discoveries or through the acquisition of additional data layers (e.g. high-resolution
591 backscatter, resistivity or self-potential data). It is expected that not all mounds within the high-priority

592 cluster are associated with SMS edifices and that additional data layers will improve the certainty of the
593 automated SMS prediction. Overall, a more diversified dataset measured at numerous SMS sites across
594 the global MORs will only help improve our understanding of SMS predictors and improve future
595 developments of ML workflows.

596

597 Marine CSEM and TEM data have demonstrated additional value when conducting tonnage estimates
598 for SMS sites. However, more development is required to improve the significance of resistivity
599 models to help quantifying volumes of mineralized zones within a mound edifice. Most notably, high-
600 resolution 3D surveys using AUV technology are likely required to accurately derive spatial extensions
601 of conductive material in these remote settings. MacGregor et al. (2021) have already presented a first
602 3D application and inversion of CSEM data and others are likely to follow suit, given the increased
603 value of electrical resistivity models to constrain volumetric predictions.

604

605 **6 Conclusion**

606 A workflow to conduct automated SMS site detection using multivariate geoscientific data is presented
607 that employs a U-Net neural network to identify prominent mound-like morphologies in bathymetry
608 data. The predicted contours are subsequently integrated with other spatial data layers (e.g. AUV
609 magnetic data) to identify high-priority sites for SMS prospecting. Within the 49 km² grid of high-
610 resolution bathymetry data, 323 mounds were detected. 98 of these were classified as high priority due
611 to their architecture and magnetic signature. Moreover, from the automated analysis 14 (10 high, 4
612 medium) of the 15 known SMS sites in the TAG area were identified as either high or medium priority.
613 Only one known site was classified within the low-priority group. The high-priority sites were spatially
614 distributed into latitudinal bands, supporting the hypotheses that focused fluid-flow at depth leads to
615 linear distributions of off-axis SMS edifices in the area.

616

617 The presented workflow cannot only be used to improve analysis and interpretation of previously
618 surveyed areas, but also serve as a blueprint to optimize SMS exploration at sea. The trained model
619 can be applied on newly acquired bathymetry data in quasi real-time to determine prospective zones for
620 more detailed confirmation/visualization studies. Thus, optimizing the use of ship time and reducing
621 exploration costs. The workflow is very adaptable to include additional data layer such as backscatter,
622 self-potential, turbidity and other water column data maps if available.

623

624 Electrical resistivity models demonstrate that mineralization of SMS mounds are less homogeneous
625 than often considered. Thus, indicating that high-grade mineral contents in SMS are not equally
626 distributed across the entire mound and that tonnage estimates may be significantly overestimated.
627 Consequently, although the workflow detects many more potential SMS edifices than previously
628 known, the overall resource potential of the TAG hydrothermal field is likely lower than previously
629 assumed.

630

631 **7 Acknowledgments**

632 AH was in part funded by the Digital Earth and SMART Projects at GEOMAR Helmholtz Centre of
633 Ocean Research Kiel.

634

635 **8 References**

636 Ade-Hall, J. M., Palmer, H. C. & Hubbard, T. P. (1971). The magnetic and opaque petrological
637 response of basalt to regional hydrothermal alteration. *Geophys. J. R. Astron. Soc.* 24, 137–174.

638

639 Andersen, C., Rüpke, L., Hasenclever, J., Grevemeyer, I., Petersen, S. (2015). Fault geometry and
640 permeability contrast control vent temperatures at the Logatchev 1 hydrothermal field, Mid-
641 Atlantic Ridge. *Geology*, 43 (1): 51–54. doi: <https://doi.org/10.1130/G36113.1>

642

643 Beaulieu, S. E., E. T. Baker, C. R. German, and A. Maffei (2013). An authoritative global database for
644 active submarine hydrothermal vent fields, *Geochem. Geophys. Geosys.*, 14, 4892–4905,
645 <https://doi.org/10.1002/2013GC004998>.

646

647 Beaulieu, S.E., Baker, E.T., German, C.R. (2015). Where are the undiscovered hydrothermal vents on
648 oceanic spreading ridges? *Deep-Sea Research Part II: Topical Studies in Oceanography*, 121,
649 202-212, <https://doi.org/10.1016/j.dsr2.2015.05.001>.

650

651 Beaulieu, S.E., Szafranski, K. (2020). InterRidge Global Database of Active Submarine Hydrothermal
652 Vent Fields, Version 3.4. World Wide Web electronic publication available from [http://vents-](http://vents-data.interridge.org)
653 [data.interridge.org](http://vents-data.interridge.org) Accessed 2022-12-01.

654

655 Bouwer, L. M., Dransch, D., Ruhnke, R., Rechid, D., Frickenhaus, S., & Greinert, J. (2022). Integrating
656 data science and earth science: Challenges and solutions (L. M. Bouwer, D. Dransch, R.
657 Ruhnke, D. Rechid, S. Frickenhaus, & J. Greinert, Eds.). Springer Nature.
658 <https://doi.org/10.1007/978-3-030-99546-1>

659

660 Clague, David, et al., (2015). Processed near-bottom Sidescan Sonar Data (version 2) from the Juan de
661 Fuca Spreading Center - Endeavour Segment acquired with AUV D. Allan B. during the Zephyr
662 expedition ZPR1108 (2011). Interdisciplinary Earth Data Alliance (IEDA),
663 <https://doi.org/10.1594/IEDA/321990>.

664

665 Constable, S., Kannberg, P. K., and Weitemeyer, K. (2016). Vulcan: A deep-towed CSEM receiver,
666 *Geochem. Geophys. Geosyst.*, 17, 1042– 1064, doi:[10.1002/2015GC006174](https://doi.org/10.1002/2015GC006174).

667

668 Constable, S., Kowalczyk, P. and Bloomer, S. (2018). Measuring marine self-potential using an
669 autonomous underwater vehicle, *Geophysical Journal International*, Volume 215, Issue 1,
670 October 2018, Pages 49–60, <https://doi.org/10.1093/gji/ggy263>.

671

672 Escartín J. & Petersen S. (2017). ODEMAR AUV Abyss (GEOMAR) + shipboard Pourquoi Pas?
673 multibeam bathymetry - 13deg20'N and 13deg30'N Oceanic Core Complexes, Mid Atlantic
674 Ridge. SEANO. <https://doi.org/10.17882/48335>.

675

676 Escartin J., Mevel C., Petersen S., Bonnemains D., Cannat M., Andreani M., Augustin N., Bezos A.,
677 Chavagnac V., Choi Y., Godard M., Haaga K., Hamelin C., Ildefonse B., Jamieson J., John B.,
678 Leleu T., Macleod C. J., Massot-Campos M., Nomikou P., Olive J. A., Paquet M., Rommevaux
679 C., Rothenbeck M., Steinfuhrer A., Tominaga M., Triebe L., Campos R., Gracias N., Garcia R.
680 (2017). Tectonic structure, evolution, and the nature of oceanic core complexes and their
681 detachment fault zones (13°20'N and 13°30'N, Mid-Atlantic Ridge). *Geochemistry Geophysics*
682 *Geosystems*, 18(4), 1451-1482. Publisher's official version :
683 <https://doi.org/10.1002/2016GC006775> , Open Access version :
684 <https://archimer.ifremer.fr/doc/00376/48702/>.

685

686 Fouquet, Y., Cambon, P., Etoubleau, J., Charlou, J.L., Ondreas, H., Barriga, F.J.A.S., Cherkashov, G.,
687 Semkova, T., Poroshina, I., Bohn, M., Donval, J.P., Henry, K., Murphy, P., Rouxel, O., (2010).
688 Geodiversity of hydrothermal processes along the Mid-Atlantic Ridge and ultramafic-hosted
689 mineralization: a new type of oceanic Cu-Zn-Co-Au volcanogenic massive sulfide deposit.
690 Article *Geophys. Monogr. Ser.* 188, 321–367.

691

692 Galley, C., Lelièvre, P., Haroon, A., Graber, S., Jamieson, J., Sztikar, F., et al. (2021). Magnetic and
693 gravity surface geometry inverse modeling of the TAG active mound. *Journal of Geophysical*
694 *Research: Solid Earth*, 126, e2021JB022228. <https://doi.org/10.1029/2021JB022228>.

695

696 Gazis, I-Z., Schoening, T., Alevizos, E., Greinert, J. (2018). Quantitative mapping and predictive
697 modeling of Mn nodules' distribution from hydroacoustic and optical AUV data linked by
698 random forests machine learning, *Biogeosciences*, 15, 7347-7377, <https://doi.org/10.5194/bg-15-7347-2018>.

700

701 Gehrman, R.A.S., Haroon, A., Morton, M., Djanni, A.T., Minshull, T.A. (2020). Seafloor massive
702 sulphide exploration using deep-towed controlled source electromagnetics: navigational
703 uncertainties, *Geophysical Journal International*, Volume 220, Issue 2, Pages 1215–1227,
704 <https://doi.org/10.1093/gji/ggz513>.

705

706 Gehrman, R., North, L. J., Graber, S., Sztikar, F., Petersen, S., Minshull, T. A., & Murton, B. J. (2019).
707 Marine mineral exploration with controlled source electromagnetics at the TAG hydrothermal
708 field, 26° N Mid-Atlantic Ridge. *Geophysical Research Letters*, 46, 5808–5816.
709 <https://doi.org/10.1029/2019GL082928>.

710

711 Gehrman, R.A.S. (2019): Controlled-source electromagnetic data from the TAG hydrothermal field,
712 26N Mid-Atlantic Ridge. PANGAEA, <https://doi.org/10.1594/PANGAEA.899073>, Supplement
713 to: Gehrman, Romina A S; North, Laurence J; Graber, Sebastian; Sztikar, Florent; Petersen, S;
714 Minshull, Tim A; Murton, Bramley J (2019): Marine Mineral Exploration With Controlled

715 Source Electromagnetics at the TAG Hydrothermal Field, 26°N Mid-Atlantic Ridge.
716 Geophysical Research Letters, 46(11), 5808-5816, <https://doi.org/10.1029/2019GL082928>
717

718 Graber, S., Petersen, S., Yeo, I., Sztikar, F., Klischies, M., Jamieson, J., et al. (2020). Structural control,
719 evolution, and accumulation rates of massive sulfides in the TAG hydrothermal field.
720 *Geochemistry, Geophysics, Geosystems*, 21, e2020GC009185.
721 <https://doi.org/10.1029/2020GC009185>.
722

723 Hannington, M., Jamieson, J.W., Monecke, T., Petersen, S., Beaulieu, S. (2011). The abundance of
724 seafloor massive sulfide deposits, *Geology*, 39, 1155-1158, <https://doi.org/10.1130/G32468.1>.
725

726 Haroon, A., Hölz, S., Gehrman, R.A.S., Attias, E., Jegen, M., Minshull, T.A., Murton, B.J. (2018).
727 Marine dipole-dipole controlled source electromagnetic and coincident-loop transient
728 electromagnetic experiments to detect seafloor massive sulphides: effects of three-dimensional
729 bathymetry, *Geophysical Journal International*, Volume 215, Issue 3, Pages 2156–2171,
730 <https://doi.org/10.1093/gji/ggy398>.
731

732 Honsho, C., Ura, T., & Kim, K. (2013). Deep-sea magnetic vector anomalies over the Hakurei
733 hydrothermal field and the Bayonnaise knoll caldera, Izu-Ogasawara arc, Japan. *Journal of*
734 *Geophysical Research: Solid Earth*, 118, 5147–5164. <https://doi.org/10.1002/jgrb.50382>.
735

736 Hu, Fan, Gui-Song Xia, Jingwen Hu, and Liangpei Zhang (2015). Transferring Deep Convolutional
737 Neural Networks for the Scene Classification of High-Resolution Remote Sensing Imagery
738 *Remote Sensing* 7, no. 11: 14680-14707. <https://doi.org/10.3390/rs71114680>.
739

740 Humphris, S. E., Herzig, P. M., Miller, D. J., Alt, J. C., Becker, K., Brown, D., et al. (1995). The
741 internal structure of an active sea-floor massive sulphide deposit. *Nature*, 377(6551), 713–716.
742 <https://doi.org/10.1038/377713a0>
743

744 Hübscher, C., Beier, C. (2022). Multibeam bathymetry processed data (EM 120 echosounder &
745 Kongsberg EM 122 dataset compilation) of RV METEOR during cruise M79/2, M113/1 &
746 M128, Azores Plateau between the Terceira Rift and the East Azores Fracture Zone, North
747 Atlantic Ocean. PANGAEA, <https://doi.org/10.1594/PANGAEA.945528>.
748

749 Ishizu, K., Goto, T., Ohta, Y., Kasaya, T., Iwamoto, H., Vachiratienchai, C., et al. (2019). Internal
750 Structure of a Seafloor Massive Sulfide Deposit by Electrical Resistivity Tomography, Okinawa
751 Trough. *Geophysical Research Letters*, 46, 11025– 11034.
752 <https://doi.org/10.1029/2019GL083749>
753

754 Jamieson, J.W., Clague, D.A., Hannington, M.D. (2014). Hydrothermal sulfide accumulation along the
755 Endeavour Segment, Juan de Fuca Ridge, *Earth and Planetary Science Letters*, 395, 136-148,
756 <http://dx.doi.org/10.1016/j.epsl.2014.03.035>.
757

758 Jamieson, J.W. & Gartman, A. (2020). Defining active, inactive, and extinct seafloor massive sulfide
759 deposits, *Marine Policy*, 117, 103926, <https://doi.org/10.1016/j.marpol.2020.103926>.
760

761 Juliani, C., Juliani, E. (2021). Deep learning of terrain morphology and pattern discovery via network-
762 based representational similarity analysis for deep-sea mineral exploration, *Ore Geology*
763 *Reviews*, 129, 103936, <https://doi.org/10.1016/j.oregeorev.2020.103936>.

764

765 Keohane, I., and White, S. (2022). "Chimney Identification Tool for Automated Detection of
766 Hydrothermal Chimneys from High-Resolution Bathymetry Using Machine Learning"
767 *Geosciences* 12, no. 4: 176. <https://doi.org/10.3390/geosciences12040176>.

768

769 Key, K. (2016). MARE2DEM: a 2-D inversion code for controlled-source electromagnetic and
770 magnetotelluric data, *Geophysical Journal International*, Volume 207, Issue 1, Pages 571–588,
771 <https://doi.org/10.1093/gji/ggw290>

772

773 Knott, R., Fouquet, Y., Honnorez, J., Pertersen, S., Bohn, M. (1998). Petrology of hydrothermal
774 mineralization: A vertical section through the TAG mound. *Proceedings of the Ocean Drilling
775 Program: Scientific Results*, 158, 5-26, <https://doi.org/10.2973/odp.proc.sr.158.201.1998>.

776

777 Koedel, U. *et al.* (2022). The Digital Earth Smart Monitoring Concept and Tools. In: Bouwer, L.M.,
778 Dransch, D., Ruhnke, R., Rechid, D., Frickenhaus, S., Greinert, J. (eds) Integrating Data
779 Science and Earth Science. SpringerBriefs in Earth System Sciences. Springer, Cham.
780 https://doi.org/10.1007/978-3-030-99546-1_6.

781

782 MacGregor, L., Kowalcyk, P., Galley, C., Weitemeyer, K., Bloomer, S., Phillips, N., Proctor, A. (2021).
783 Characterization of Seafloor Mineral Deposits Using Multiphysics Datasets Acquired from an
784 AUV, *First Break*, 39 (8), 63-69, <https://doi.org/10.3997/1365-2397.fb2021062>.

785

786 Morgan, L. A., (2012). Geophysical characteristics of volcanogenic massive sulfide deposits, in
787 Volcanogenic Sulfide Occurrence Model, pp. 115–131, eds ,Pat Shanks W.C., III & Thurston, R.,
788 USGS.

789

790 Murton, B.J. and Shipboard Scientific Party (2018). Cruise Report: Expedition JC138: 29th June-8th
791 August 2016, Mid Atlantic Ridge, 26°8.38'N; 44°49.92'W, National Oceanography Centre
792 Southampton, Southampton, pp. 285.
793 https://www.bodc.ac.uk/resources/inventories/cruise_inventory/reports/jc138.pdf (accessed 29
794 November 2022).

795

796 Murton, B.J., Lehrmann, B., Dutrieux, A. M., Martins, S., Gil de la Iglesia, A., Stobbs, I.J., Barriga,
797 F.J.A.S., Bialas, J., Dannowski, A., Vardy, M.E., North, L.J., Yeo, I.A.L.M., Lusty, P.A.J.,
798 Petersen, S. (2019). Geological fate of seafloor massive sulphides at the TAG hydrothermal
799 field (Mid-Atlantic Ridge), *Ore Geology Reviews*, 107, 903-925,
800 <https://doi.org/10.1016/j.oregeorev.2019.03.005>.

801

802 Müller, H., Schwalenberg, K., Barckhausen, U. (2023). Magnetic and electromagnetic exploration of
803 SMS deposits; perspectives and frontiers, 84th EAGE Annual Conference & Exhibition, Volume
804 2023, p. 1-5, <https://doi.org/10.3997/2214-4609.2023101269>.

805

806 Olakunle, O.K., Ajibola, L.M., Muhammad, I.H. *et al.* (2021). Massive seafloor mounds depict
807 potential for seafloor mineral deposits in the Great South Basin (GSB) offshore New Zealand.
808 *Sci Rep* 11, 9185. <https://doi.org/10.1038/s41598-021-88620-x>.

809

810 Petersen, S. and Shipboard Scientific Party (2016). *RV METEOR Cruise Report M127 Metal fluxes and
811 Resource Potential at the Slow-spreading TAG Midocean Ridge Segment (26°N, MAR) – Blue
812 Mining@Sea, Bridgetown (Barbados) – Ponta Delgada (Portugal), 25.05.-28.06.2016.*

813 GEOMAR Report, N. Ser. 032 . GEOMAR Helmholtz-Zentrum für Ozeanforschung Kiel, Kiel,
814 87, 69 pp. DOI [10.3289/GEOMAR_REP_NS_32_2016](https://doi.org/10.3289/GEOMAR_REP_NS_32_2016).
815

816 Petersen, Sven (2019). Bathymetric data products from AUV dives during METEOR cruise M127
817 (TAG Hydrothermal Field, Atlantic). GEOMAR - Helmholtz Centre for Ocean Research Kiel,
818 PANGAEA, <https://doi.org/10.1594/PANGAEA.899415>.
819

820 Reeck, K., Müller, H., Hölz, S., Haroon, A., Schwalenberg, K. and Jegen, M. (2020). Effects of
821 metallic system components on marine electromagnetic loop data. *Geophysical Prospecting*, 68:
822 2254-2270. <https://doi.org/10.1111/1365-2478.12984>.
823

824 Rona, P. A. (1978). Criteria for recognition of hydrothermal mineral deposits in oceanic crust.
825 *Economic Geology*; 73 (2): 135–160. doi: <https://doi.org/10.2113/gsecongeo.73.2.135>
826

827 Rona, P. A. (1980). TAG hydrothermal Field: Mid-Atlantic Ridge crest at latitude 26°N. Geological
828 Society of London. *Journal* 137, 385–402, <https://doi.org/10.1144/gsjgs.137.4.038>.
829

830 Ronneberger, O., Fischer, P., Brox, T. (2015). U-Net: Convolutional Networks for Biomedical Image
831 Segmentation. In: Navab, N., Hornegger, J., Wells, W., Frangi, A. (eds) *Medical Image*
832 *Computing and Computer-Assisted Intervention – MICCAI 2015*. MICCAI 2015. Lecture
833 Notes in Computer Science(), vol 9351. Springer, Cham. [https://doi.org/10.1007/978-3-319-](https://doi.org/10.1007/978-3-319-24574-4_28)
834 [24574-4_28](https://doi.org/10.1007/978-3-319-24574-4_28).
835

836 Sinha, M.C., Patel, P.D., Unsworth, M.J. *et al.* (1990). An active source electromagnetic sounding
837 system for marine use. *Marine Geophysical Researches* 12, 59–68 .
838 <https://doi.org/10.1007/BF00310563>.
839

840 Spagnoli, G., , Hannington, M., Bairlein, K., Hördt, A., Jegen, M., Petersen , S. & Laurila, T. (2016).
841 Electrical properties of seafloor massive sulfides, *Geo Mar. Lett.*, 36, 235–245.
842

843 Swidinsky, A., Hölz, S. and Jegen, M. (2012). On mapping seafloor mineral deposits with central loop
844 transient electromagnetics, *Geophysics*, 77, 3, E171-E184. [https://doi.org/10.1190/geo2011-](https://doi.org/10.1190/geo2011-0242.1)
845 [0242.1](https://doi.org/10.1190/geo2011-0242.1)
846

847 Szitkar, F., Dymant, J., Petersen, S. *et al.* (2019). Detachment tectonics at Mid-Atlantic Ridge 26°N.
848 *Sci Rep* 9, 11830. <https://doi.org/10.1038/s41598-019-47974-z>.
849

850 Villinger, Heinrich; Strack, Anne; Gaide, Stefanie; Thal, Janis (2018). Gridded bathymetry of North
851 Pond (MAR) from multibeam echosounder EM120 and EM122 data of cruises MSM20/5
852 (2012) and MSM37 (2014). Department of Geosciences, Bremen University, PANGAEA,
853 <https://doi.org/10.1594/PANGAEA.889439>.
854
855
856

Table A1: List of open-access bathymetry data used for training the U-Net.

Index	Extent		Resolution	Source / Reference
	Longitude Min. Longitude Max.	Latitude Min. Latitude Max		
1	-44.99625 -44.69042	25.98625 26.28625	~ 90 m	Multibeam Mosaic https://www.ncei.noaa.gov/maps/bathymetry/
2	-43.23542 -41.31541	29.69375 30.78042	~ 90 m	Multibeam Mosaic https://www.ncei.noaa.gov/maps/bathymetry/
3	-34.45958 -33.12792	35.45792 37.50708	~ 90 m	Multibeam Mosaic https://www.ncei.noaa.gov/maps/bathymetry/
4	-27.14292 -23.76958	61.70625 63.44625	~ 90 m	Multibeam Mosaic https://www.ncei.noaa.gov/maps/bathymetry/
5	-45.21799 -44.40485	25.77404 26.54754	~ 30 m	Petersen (2019) https://doi.org/10.1594/PANGAEA.899415
6	-44.85162 -44.75758	26.10058 26.18684	~ 2 m	Petersen (2019) https://doi.org/10.1594/PANGAEA.899415
7	-44.97116 -44.86794	13.27914 13.34156	~ 2m	Escartin & Petersen (2017) and Escartin et al. (2017)
8	-45.00966 -44.88124	13.48664 13.52226	~ 2 m	Escartin & Petersen (2017) and Escartin et al. (2017)
9	-46.45929 -45.81298	22.36806 23.05779	~ 10 m	Villinger et al. (2018) https://doi.org/10.1594/PANGAEA.889439
10	-34.99333 -31.87833	56.69666 58.00000	~ 90 m	Multibeam Mosaic https://www.ncei.noaa.gov/maps/bathymetry/
11	-42.40119 -41.72925	29.82935 30.36156	~ 90 m	Multibeam Mosaic https://www.ncei.noaa.gov/maps/bathymetry/
12	-129.1490 -129.0070	47.88199 48.08900	~ 1 m	Clague et al. (2015) http://get.iedadata.org/doi/321990
13	-177.1383 -176.3533	-23.0983 -21.5792	~ 90 m	Multibeam Mosaic https://www.ncei.noaa.gov/maps/bathymetry/
14	-29.93012 -22.78952	35.99997 39.50023	~ 45 m	Hübscher & Beier (2022) https://doi.pangaea.de/10.1594/PANGAEA.945528

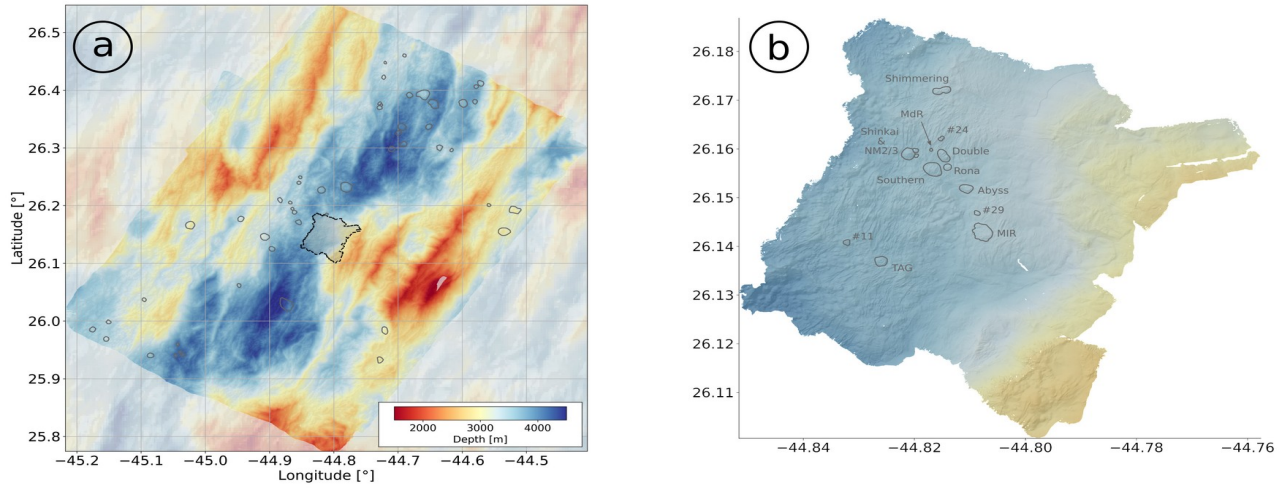


Figure 1: Bathymetry maps of the study area. (a) GEBCO bathymetry (shaded map) overlain by the ship-based bathymetry data acquired during RV Meteor cruise M127 with a spatial resolution of 30 m. Gray outlines denote visible mound structures whereas the black outlined region denotes the high-resolution bathymetry survey illustrated in (b). (b) AUV bathymetry data acquired with a spatial resolution of 2 m using the same color scale as in (a). Known SMS mounds are outlined and labeled as depicted by Graber et al. (2020).

859 |
860 |

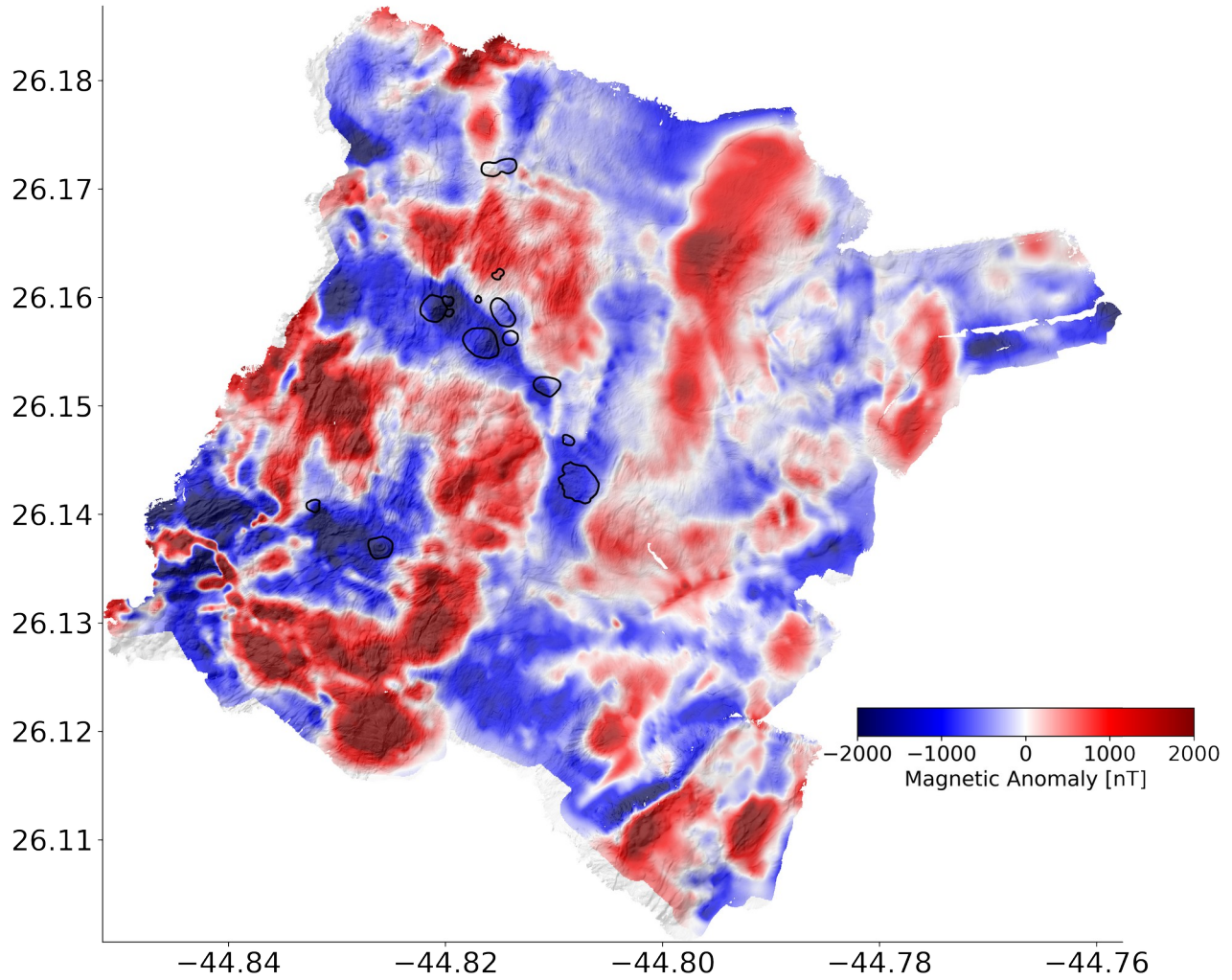


Figure 2: Overlay map of the hillshade bathymetry (2 m resolution) and the magnetic anomaly map with 10 m spatial resolution from Pedersen (2016). Outlined in black are the known SMS mounds depicted by Graber et al. (2020).

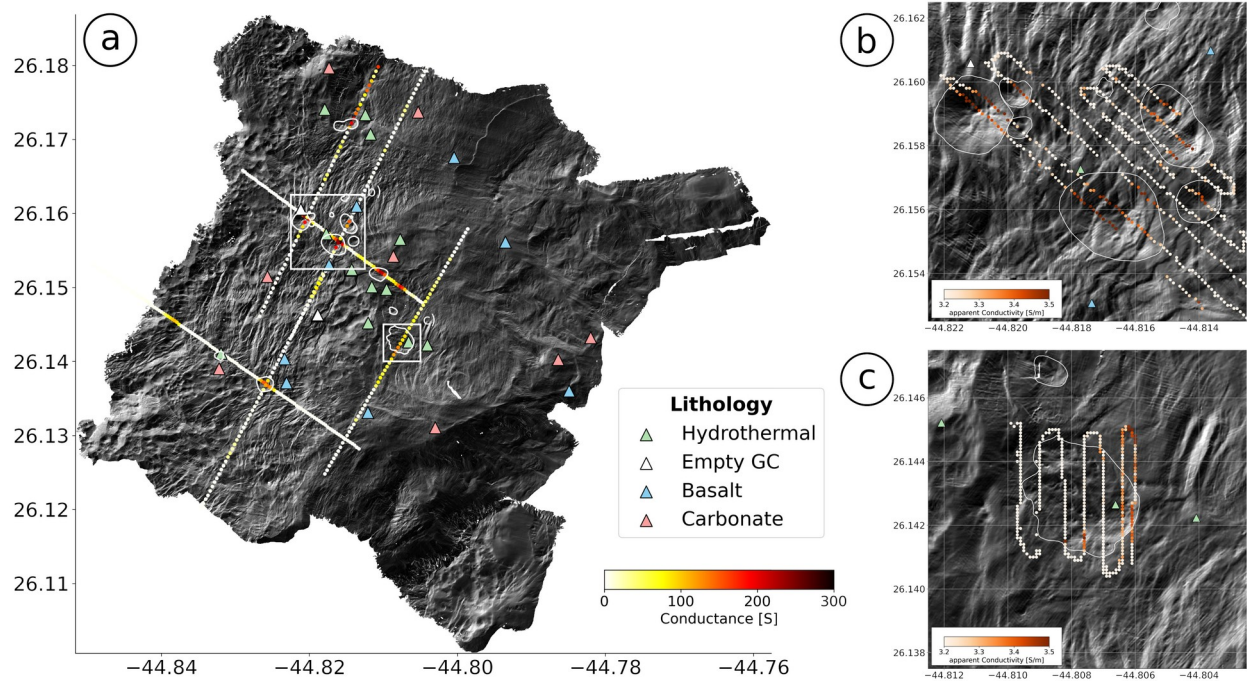


Figure 3: (a) Hillshade map of the bathymetry data with a spatial resolution of 2 m. Computed electrical conductance values derived from 2D CSEM resistivity models of Gehrman et al. 2019 are displayed with color-coded markers. Light colors denote a low and hot colors a high conductance. (b) Zoom-in of the Three-Mound region overlain by the transformed apparent conductivity values obtained by TEM measurements. (c) Same as (b) but for the MIR zone. Outlines of the mounds denote the manually-annotated lateral mound dimensions from Graber et al. (2020). Triangular markers in (a) through (c) illustrate the locations of the 3 m gravity cores and the lithology observed within the core samples (Petersen, 2016).

864
 865
 866
 867
 868

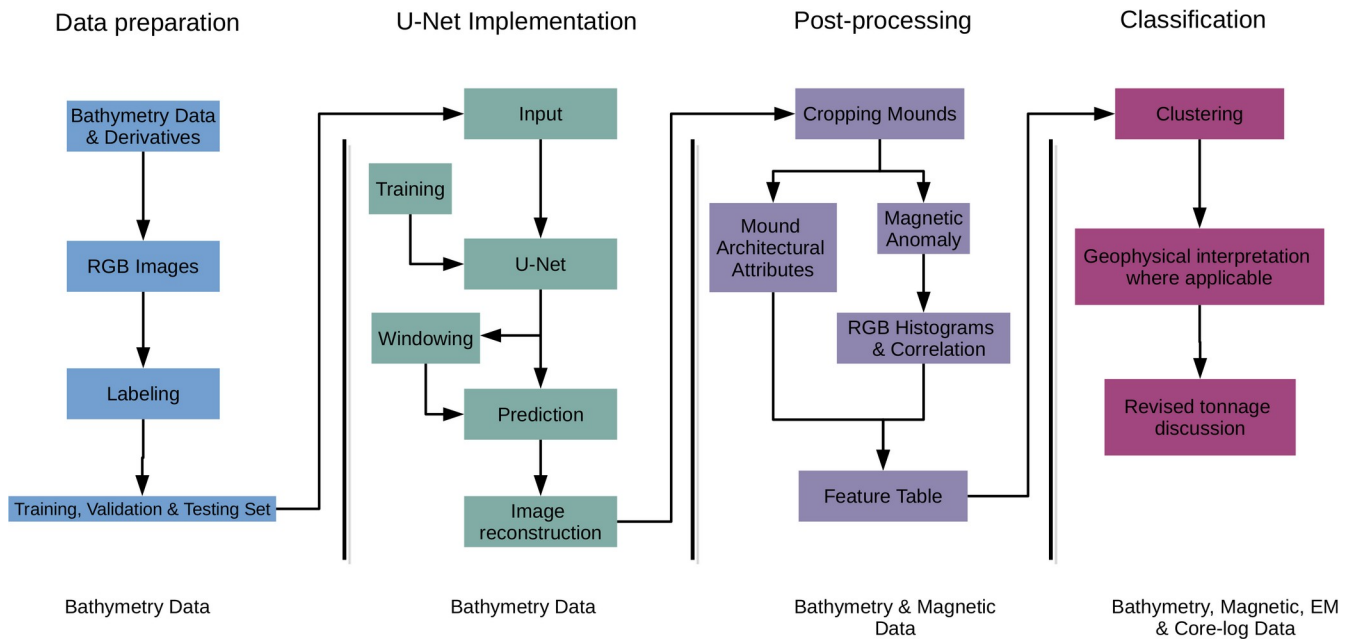


Figure 4: Schematic of the applied workflow including all relevant steps applied, i.e. data preparation, U-Net implementation, post-processing and classification.

870

871 |

872 |

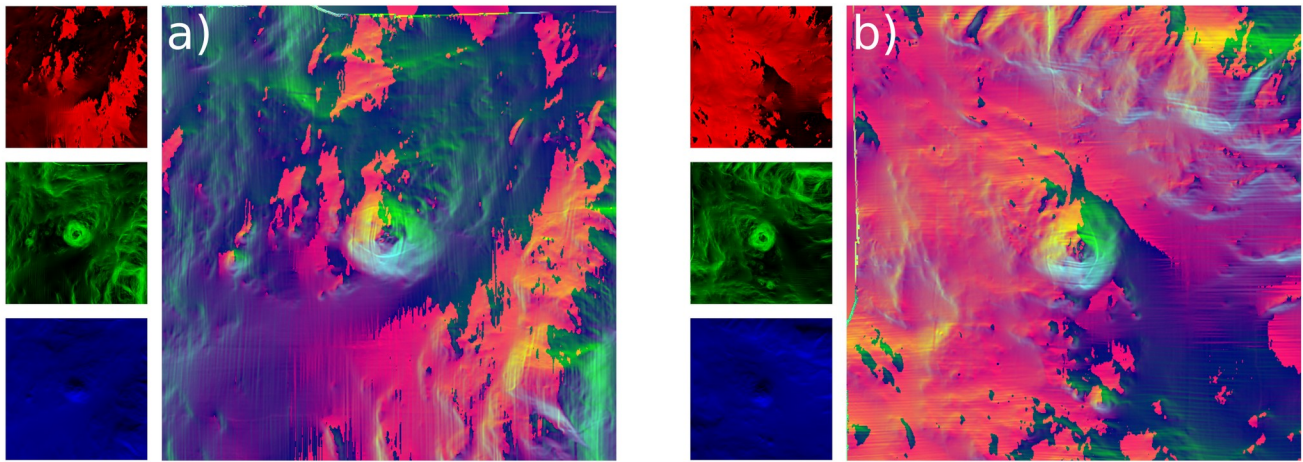


Figure 5: Image unification example of relevant bathymetry features into a common visual representation that is generically applicable to coherently address bathymetry data acquired at different regions across the globe. The aspect, slope, and ∂y derivative of the bathymetry are mapped onto the red, green and blue channels of a standardized 0-255 RGB image (left column of each panel). In this representation, mounds appear directionally invariant with coherent color representation. (a) The original input data and (b) the original input data rotated by 90° . Contrarily, the background bathymetry differs based on the predominant strike direction of the seafloor morphology, whereas prominent mound features remain rotational invariant.

873

874

875

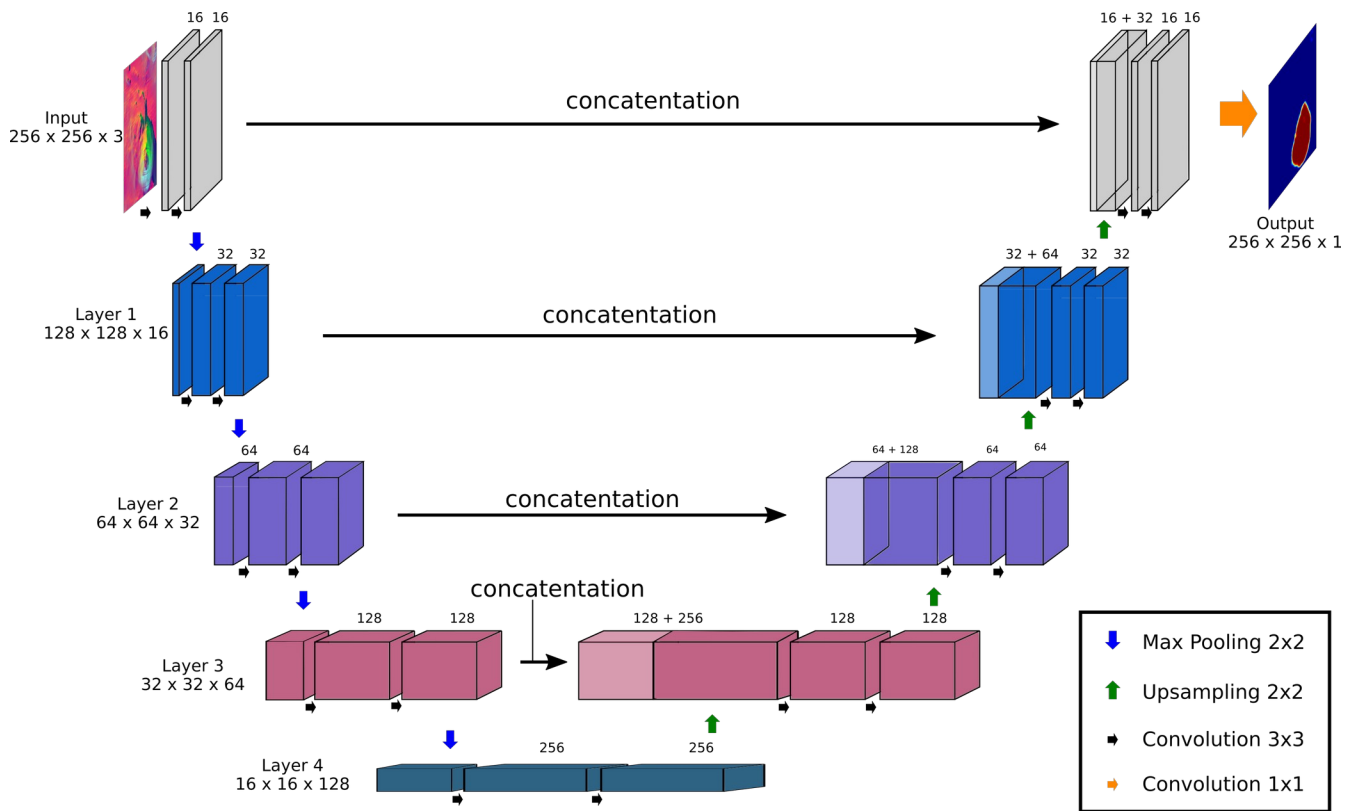


Figure 6: Schematic of the U-Net architecture used for semantic segmentation of the bathymetry data (modified after Ronneberger et al., 2015).

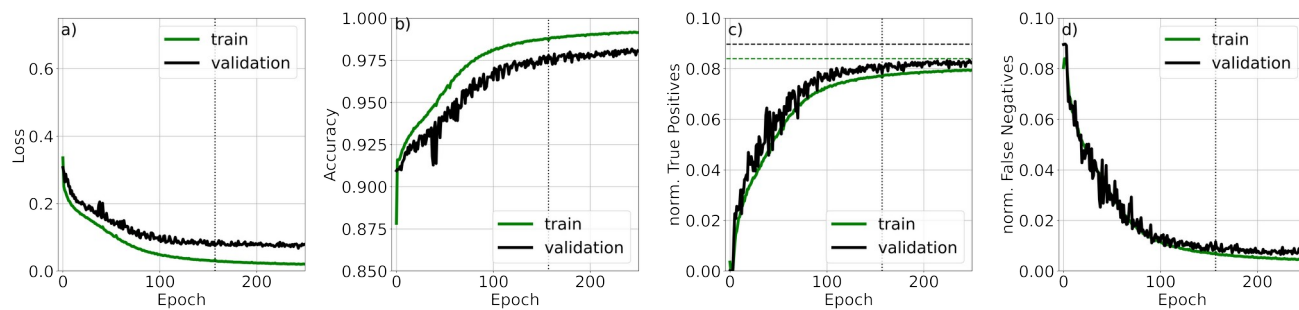


Figure 7: (a) Binary cross-entropy loss function used during training (green) and validation (black). Additional metrics, i.e. (b) accuracy, (c) true positives and (d) false negatives are also used to assess the model performance. Note that true positives and false negatives are normalized to represent percentages of of pixels per image. The vertical dotted line denotes the point of early stopping whereas the horizontally dashed lines in (c) represent the average number of pixels affiliated with mound structure within training and validation data.

880 |

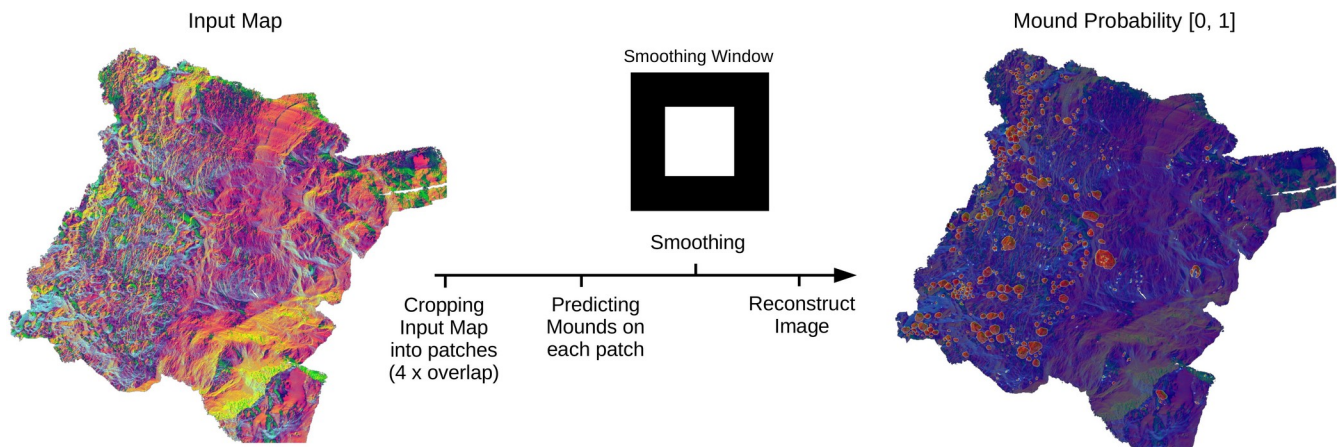
881 |

882 |

883 |

884 |

885 |



Figsize=(4608, 5120)

Figure 8: Workflow of mound prediction for the AUV bathymetry raster. The pre-processed AUV bathymetry map is cropped into overlapping 256 x 256 patches, which are presented to the U-Net for prediction. The output is smoothed using displayed window where pixels within the black region are neglected due to edge effects that deteriorate predictions (as observed within the testing phase). The right panel shows the final prediction map that is utilized for further processing.

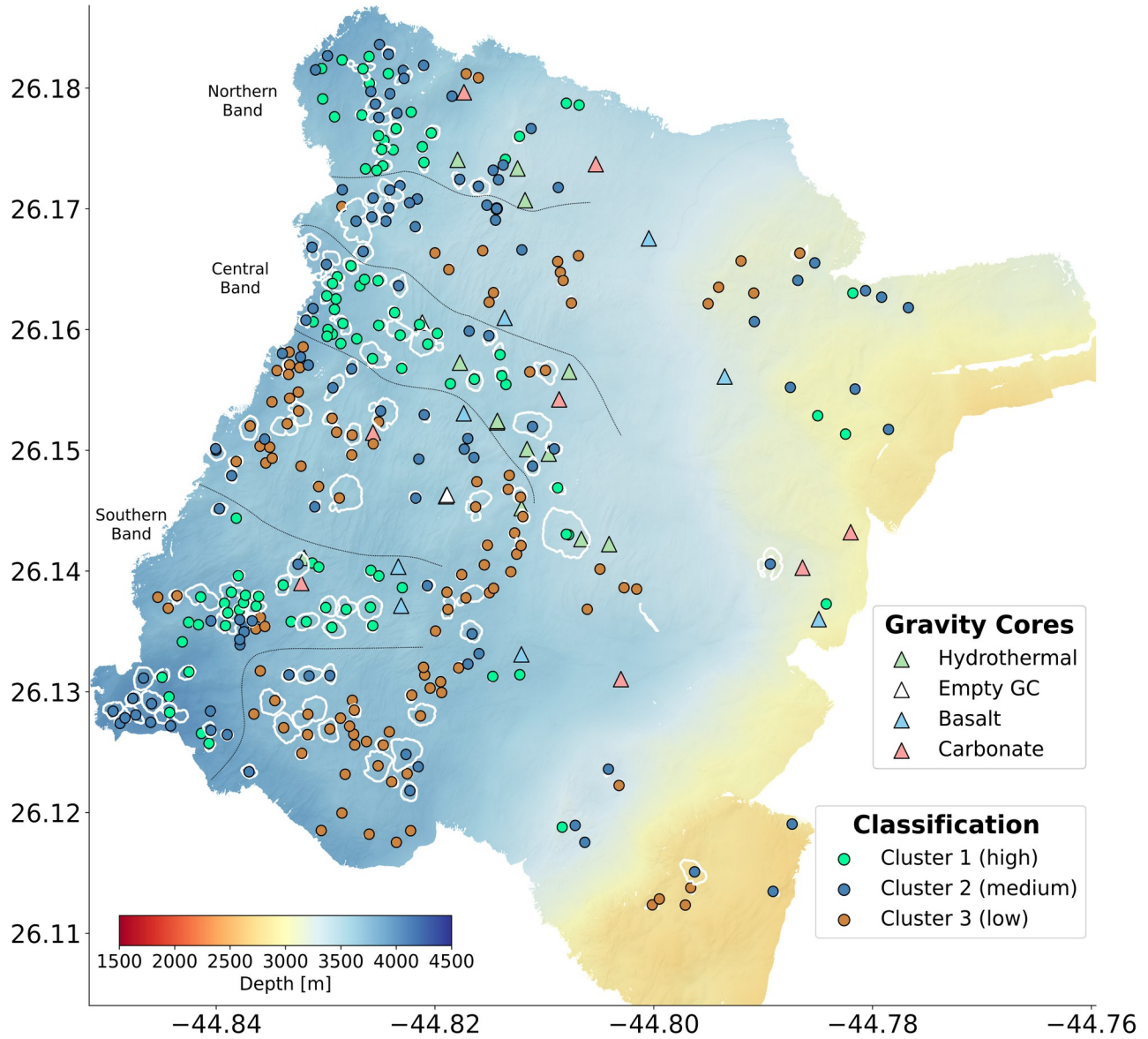


Figure 9: Bathymetry map containing the 323 mounds with a lateral of footprint greater than 290 pixels (1040 m^2) as predicted by the U-Net. The mounds are illustrated by white contours and are classified as either Cluster 1 (high priority), Cluster 2 (medium priority) or Cluster 3 (low priority). Dotted gray lines illustrate the interpreted boundaries of the three latitudinal bands containing hydrothermal edifices.

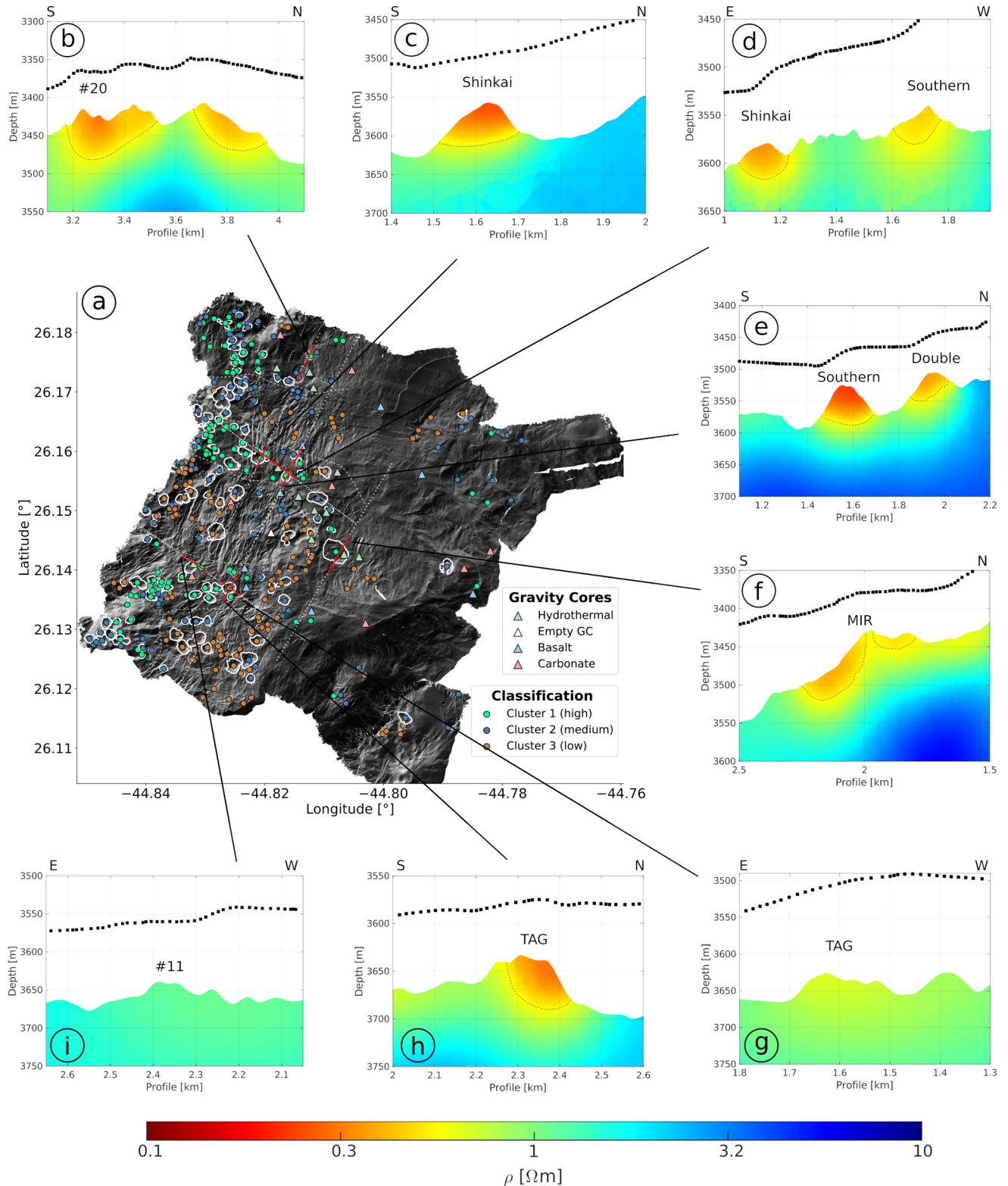


Figure 10: (a) Hillshade bathymetry data with classified mounds as illustrated in Fig. 9. Panels (b) through (i) show electrical resistivity models for each of the high priority mounds intersecting a CSEM profile. The lateral extent of each profile is illustrated by red lines in (a). In (b) through (I), red color shading indicates low resistivity (mineralization), whereas green/blue are more resistive background basalts. Black markers denote transmitter positions along profile.